ATLAS NOTE

ATL-PHYS-PUB-2013-014

October 9, 2013
Revised May 13, 2014

Projections for measurements of Higgs boson cross sections, branching ratios and coupling parameters with the ATLAS detector at a HL-LHC

The ATLAS Collaboration

Abstract

Studies are presented on the prospects for measuring Higgs boson production cross sections times branching ratios, and determining couplings to individual fermions and bosons in 14 TeV proton-proton collisions at the LHC with 300 fb^{-1} and at the HL-LHC with 3000 fb^{-1}. Several studies already presented at the 2012 European Strategy meeting are updated. In addition first analyses are presented of $H \to Z\gamma$, of ZH production with $H \to$ invisible final states, and on the measurement of the Higgs width from the interference in $H \to \gamma\gamma$.

Figure 19 has been updated to correct an error in the calculation of the ATLAS upper limits on the dark matter-nucleon scattering cross section in the Higgs-portal model; the corrected limits are about 0.98 (left) and 0.86 (right) times the previous ones. The result from CDMS II has also been updated to the latest one, and several references have been updated. The limits on the Higgs boson invisible branching ratio are not affected.

1 Introduction

One of the main motivations for an upgrade of the LHC to deliver high lumiminosity, HL-LHC, is to enable precise measurements of the Higgs boson properties. In the Standard Model, all properties of the Higgs boson are defined once its mass is known. However, this model leaves many open questions such as the hierarchy problem or the nature of dark matter. Many alternative theories addressing these issues make different predictions for the properties of one or more Higgs bosons. Precise measurements in the Higgs sector are therefore a priority in the future programme of particle physics. The ATLAS collaboration presented a preliminary set of studies for the update of the European Strategy for Particle Physics [1] which are included in the briefing book [2]. They also comprise the physics case in the ATLAS Phase-II upgrade Letter of Intent [3].

The European Strategy group recommended the high luminosity upgrade of the LHC as the highest priority. However, further analyses are needed to define the performance requirements needed for the detector upgrade. To achieve these goals, CERN and ECFA have organised a workshop in October 2013. ATLAS studies of the projected precision of measurements of the Higgs boson production cross section times branching ratios and their interpretation in terms of Higgs boson couplings are ongoing, and this note summarises the current status as an input to the ECFA HL-LHC workshop.

The present LHC programme is expected to deliver a total integrated luminosity of about 300 fb^{-1} by the year 2022. The peak instantaneous luminosity will be in the range 2 to 3$\times 10^{34}$ cm^{-2} s^{-1}. The luminosity will decrease from the peak value during a fill, so this sample is assumed to have a typical average number of pile-up events per bunch crossing, which is denoted here by μ_{pu}, of 50–60. The HL-LHC would deliver a total luminosity of about 3000 fb^{-1}, at a peak levelled luminosity of 5×10^{34} cm^{-2} s^{-1}, with a value of $\mu_{\mathrm{pu}} = 140$.

The detector design for the high luminosity phase is not yet completely defined and it will take years to adapt and optimise the event reconstruction software to the high-pile-up conditions. The goal is that the performance of the new detector in the harsh conditions of the high luminosity phase will not be worse than the performance of the current detector with $\mu_{\mathrm{pu}} \approx 20$. For the input to the European Strategy group, the particle level quantities were modified by applying efficiency and resolution ("smearing") functions to physics objects [4] which were derived from samples using the Run-1 ATLAS detector with various values of μ_{pu}, up to a maximum average of $\mu_{\mathrm{pu}} = 69$. A major improvement is that many of these functions have now been updated with the results of full simulation of the Phase-I detector with μ_{pu} values up to 80, and the Phase-II detector with μ_{pu} values of 80, 140 and 200 [5].

The rates of tagging b, c and light flavour jets have been parametrised using one of the more robust tagging algorithms at a 70% efficiency working point for b-jets produced in $t\bar{t}$ events. It is expected that more sophisticated algorithms will give even better light jet rejection for the same efficiency, but they are not yet optimised for the Phase-II detector. A higher efficiency working point would also be preferred for some of the statistics limited channels presented here, since the light-jet rejection rate is better than with the Run 1 detector, despite the high pile-up.

A detailed reparametrisation of the $E_{\mathrm{T}}^{\mathrm{miss}}$ performance has been implemented based on full simulation up to the highest luminosities. This results in a better performance than inferred from an extrapolation of lower luminosity samples that was used previously. The new function also applies a more realistic shape for fluctuations leading to fake $E_{\mathrm{T}}^{\mathrm{miss}}$. The improved Phase-II tracker provides superior muon resolution, and this is now taken into account.

The electron, photon and tau identification and energy resolution performance have not been changed from the previous studies. In the case of the photon performance, the functions are based on the performance in samples with $\mu_{\mathrm{pu}} = 40$, 60 and 80, and it is assumed that detector improvements will mitigate the effects of increased pile-up at the level of $\mu_{\mathrm{pu}} \approx 140$. The jet energy resolution expectations are also retained from previous studies, as are the p_{T} thresholds needed to control the rate of fake jets from

pile-up.

This note presents an update of the studies in Ref. [2], as well as a new analysis of the $H \to Z\gamma$ channel. The measurements of the cross sections times branching ratio are expressed in terms of the ratio to the Standard Model expectation, $\mu = \sigma/\sigma_{\rm SM}$. The expected precision is given as the relative uncertainty in the signal strength, $\Delta\mu/\mu$. These measurements are then interpreted in terms of the Higgs boson couplings to elementary particles.

A Standard Model Higgs boson has a width much too narrow to be measured directly at the LHC. A new method has been proposed recently to infer the Higgs width from the mass shift due to interference of the $gg \to H \to \gamma\gamma$ and $gg \to \gamma\gamma$ amplitudes [6, 7]. A first study using this method in the future LHC runs is presented in this note. The prospects for constraints from the search for ZH with $H \to$ invisible final states are also explored.

2 $H \to ZZ$

The $H \to ZZ \to \ell^+\ell^-\ell^+\ell^-$ decay offers a very clean final state signature with excellent signal to background ratio in the HL-LHC environment. The large number of events in a 3000 fb^{-1} sample allows the study of all the Higgs production modes separately using this channel, adding important sensitivity to the measurement of Higgs coupling parameters.

The analysis follows the selection criteria used in the analysis of the full Run 1 data set [8]. The efficiency of requiring confirmation of the calorimeter jet by the presence of a matching track-jet with $p_{\rm T} > 5$ GeV is taken into account (track confirmation) for jets falling inside the ID acceptance and their $p_{\rm T}$ thresholds are tuned [1] to allow at most a 1% fake rate from pile-up with $\mu_{\rm pu} = 140$. The main irreducible background is $q\bar{q} \to ZZ$ di-boson production. The relevant reducible background processes, which are Z+jets, $Zb\bar{b}$ and $t\bar{t}$, are accounted for conservatively as an additional 50% of the irreducible background.

2.1 Event selection

Events are selected in categories that are designed to minimise the cross-talk between different production mechanisms. The aim is to assign events in the following order: $t\bar{t}H$, ZH, WH and vector boson fusion (VBF) production. The remaining events are allocated to the gluon-gluon fusion (ggF) category.

The event selection to define 4-lepton final states follows Ref. [8]. A lepton quadruplet is formed from two pairs of same-flavor and opposite-sign leptons. The dilepton pair with mass closer to that of the Z boson is required to have a mass between 50 and 115 GeV. The mass of the other pair is required to be between 12 and 115 GeV. Quadruplets with same-flavor, opposite-sign lepton pairs with mass less that 5 GeV are excluded to avoid J/ψ contamination. Thresholds of 20, 15, 10 and 6 GeV (7 GeV for electrons) are applied to the lepton $p_{\rm T}$. At this stage, good agreement is found between the analysis based on smeared truth quantities and one obtained from full simulation.

The last requirement in the standard analysis is lepton isolation, which can not be inferred from only the generator level information of the hard scattering event without pile-up. However, lepton isolation is very important for the suppression of reducible backgrounds. In particular, for leptons with $p_{\rm T} \leq 10$ GeV, it is expected that high pile-up will induce some loss of efficiency compared to the Run 1 performance (95% at $p_{\rm T} \simeq 20$ GeV, 90% at $p_{\rm T} \simeq 10$ GeV). In order to maintain similar suppression of the reducible backgrounds at a luminosity of 5×10^{34} cm^{-2} s^{-1}, a 20% inefficiency to account for isolation requirements is assumed for leptons with $p_{\rm T} < 20$ GeV.

[1] To ensure at most 1% contribution from pile-up jets, throughout this note, the requirements are $p_{\rm T} > 41$ GeV for $|\eta| < 2.1$, $p_{\rm T} > 77$ GeV for $2.1 \leq |\eta| < 2.8$, $p_{\rm T} > 74$ GeV for $2.8 \leq |\eta| < 3.2$, $p_{\rm T} > 50$ GeV for $3.2 \leq |\eta| < 4.5$.

2.1.1 $t\bar{t}H, H \to ZZ$

The selection of $t\bar{t}H$ events exploits the production of two b-jets from the decays of the top quarks by requiring at least one b-tagged jet. To account for the leptonic W decays, one additional lepton with $p_{\mathrm{T}} > 8$ GeV is also required. If no lepton is present, at least four additional jets are required in order to account for hadronic decays of both W bosons and classify the event in the ttH category. Figure 1 shows the distribution of the number of b-tagged jets before requiring at least one tag, as well as the distribution of the number of the additional leptons (excluding the ones coming from the Higgs decay) in events where at least one b-tagged jet is present, for the different Higgs production mechanisms and the background. Together with the initial four-lepton requirement, the criteria imposed in this analysis are sufficient to select a very clean $t\bar{t}H$ sample.

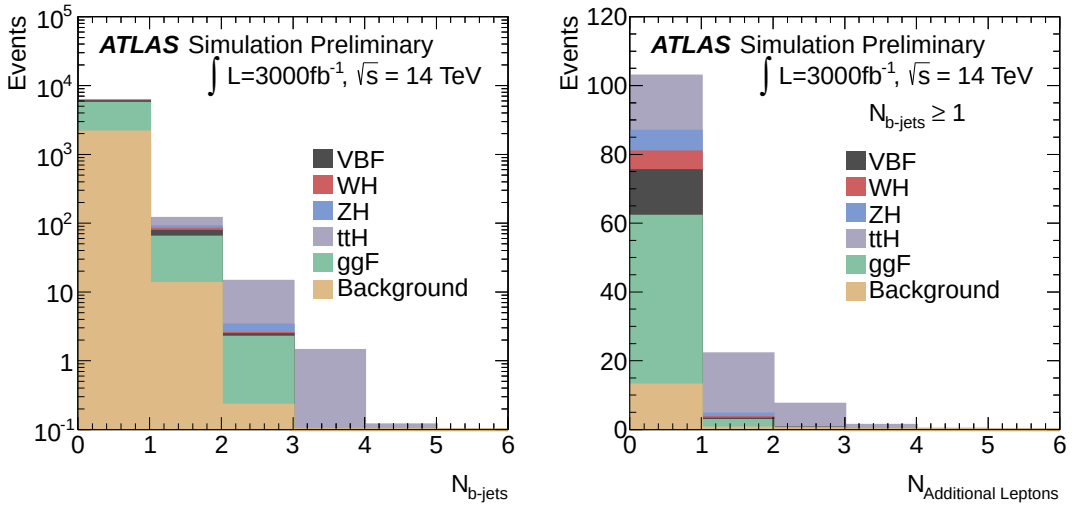

(a) (b)

Figure 1: The distribution of the number of b-tagged jets (a) and the number of additional leptons in events with at least one b-tagged jet (b), for different Higgs production mechanisms and ZZ background.

2.1.2 $VH, H \to ZZ$ where $V = W, Z$

Events that contain two additional same-flavour opposite-sign leptons and do not fall in the previous category are classified as ZH, $H \to ZZ$ candidates. In order to reduce the rate of $t\bar{t}H$ events that fail the b-tagging requirement then fall into this category, the mass of the additional lepton pair is required to be within 15 GeV to the nominal Z boson mass. Remaining events which contain one additional lepton with $p_{\mathrm{T}} > 8$ GeV are then classified in the WH category.

2.1.3 Vector Boson Fusion, $H \to ZZ$

Events that are not selected by the previous requirements fall in the VBF or ggF categories. A search for at least two additional jets is then performed. A jet pair is accepted if the η difference between the jets is above $\Delta\eta > 3$. The invariant mass, m_{jj}, of the two highest p_{T} jets is then used as a discriminant for the VBF category; the event is assigned to the VBF category if $m_{jj} > 350$ GeV. Figure 2 shows the distribution of $\Delta\eta$ and the mass m_{jj} of the selected dijet pair, for different Higgs production mechanisms and the background.

2.1.4 Gluon-gluon fusion

The gluon-gluon fusion category consists of all the events that are not tagged with the above requirements.

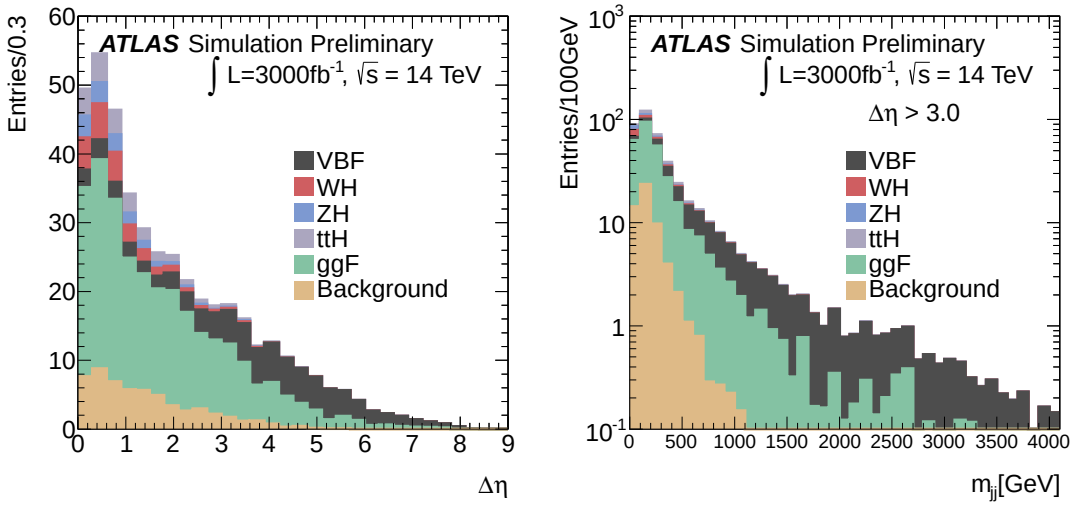

(a) (b)

Figure 2: The distribution of $\Delta\eta$ (a) and the mass m_{jj} (b) of the selected dijet pair, for different Higgs production mechanisms and background.

2.2 Systematic Uncertainties

The theoretical uncertainties on signal yields assumed in this analysis for the different production mechanisms of the Higgs boson follow Ref. [9]. The irreducible background is evaluated using side-band regions around the Higgs boson mass peak. Reducible backgrounds are also expected to be evaluated using data driven methods similar to those described in Ref. [8]. In the case where it is not possible to constrain an uncertainty with data driven methods, a 7% (35% for the VBF case) uncertainty on the background is introduced.

The detector uncertainties from lepton reconstruction and selection, affect all channels in a similar way and are assumed to be equal to those in Ref. [8]. The jet energy scale, the jet track confirmation and the b-tagging performance are the main jet related uncertainties affecting mostly the ttH and VBF categories. The main systematic uncertainty for the ttH category is due to b-tagging and the track confirmation required for the jets. However these uncertainties are small compared to the theory uncertainties. A 5% uncertainty in the b-tagging efficiency or the track confirmation inefficiency corresponds to a 2% uncertainty in the $t\bar{t}H$ event selection efficiency. The other Higgs boson production contributions and the background are also affected by the jet energy scale and resolution at a level below 10%. The dominant sources of detector related uncertainties in the VBF category are due to the jet energy scale and resolution together with uncertainties concerning the undelying event. In the current analysis it is assumed that their contribution is similar to Ref. [8]. Finally, a 3% uncertainty is assumed on the integrated luminosity.

2.3 Results

Following the event selection defined above, the mean expected event yields in each category for signal and background is given in Table 1. The yields are reported in the lepton quadruplet mass interval

between 115 and 130 GeV. The total uncertainties on the corresponding estimates are also given. Figure 3 shows the invariant mass distributions of the lepton quadruplets coming from the various Higgs production mechanisms and background for the different category selections.

Category	True Origin					
	ggF	VBF	WH	ZH	ttH	Background
ttH-like	3.1 ±1.0	0.6 ±0.1	0.6 ±0.1	1.1 ±0.2	30 ±6	1.6 ±1.0
ZH-like	0.0	0.0	0.01 ±0.01	4.4 ±0.3	1.3 ±0.3	0.06 ±0.06
WH-like	22 ±7	6.6 ±0.4	25 ±2	4.4 ±0.3	8.8 ±1.8	13 ±0.8
VBF-like	41 ±14	54 ±6	0.7 ±0.1	0.4 ±0.1	1.0 ±0.2	4.2 ±1.5
ggF-like	3380 ±650	274 ±17	77 ±5	53 ±3	25 ±4	2110 ±50

Table 1: Mean expected number of events in each category assuming $m_H = 125$ GeV and 3000 fb^{-1} of data. For each category, the expected number of events from the various Higgs production mechanisms is specified. Estimates are given in the lepton quadruplet mass interval between 115 and 130 GeV, along with their total uncertainties.

The expected relative uncertainty on the combined signal strength, μ, along with that of different production modes, is summarized in the Table 2. Results are shown for the 300 and 3000 fb^{-1} data samples. The uncertainty on μ_{ggF} is significantly reduced compared to the result using the 2011 and 2012 data and is dominated by theoretical uncertainties. With the HL-LHC a significant improvement in the VBF and VH associated production modes is obtained and makes it possible to measure the signal strength in the $t\bar{t}H$ production mode with a reasonable precision.

$\Delta\mu/\mu$	Total	Stat.	Expt. syst.	Theory
Production mode	300 fb^{-1}			
ggF	0.152	0.066	0.053	0.124
VBF	0.625	0.545	0.233	0.226
WH	1.074	1.064	0.061	0.085
$t\bar{t}$H	0.535	0.516	0.038	0.120
Combined	0.125	0.042	0.044	0.108
	3000 fb^{-1}			
ggF	0.131	0.025	0.040	0.124
VBF	0.371	0.187	0.225	0.226
WH	0.390	0.375	0.061	0.085
ZH	0.532	0.526	0.038	0.073
$t\bar{t}$H	0.224	0.184	0.034	0.120
Combined	0.100	0.016	0.036	0.093

Table 2: Expected relative uncertainties on the signal strength, for samples of 300 fb^{-1} and 3000 fb^{-1}, for the various Higgs production mechanisms and their combination.

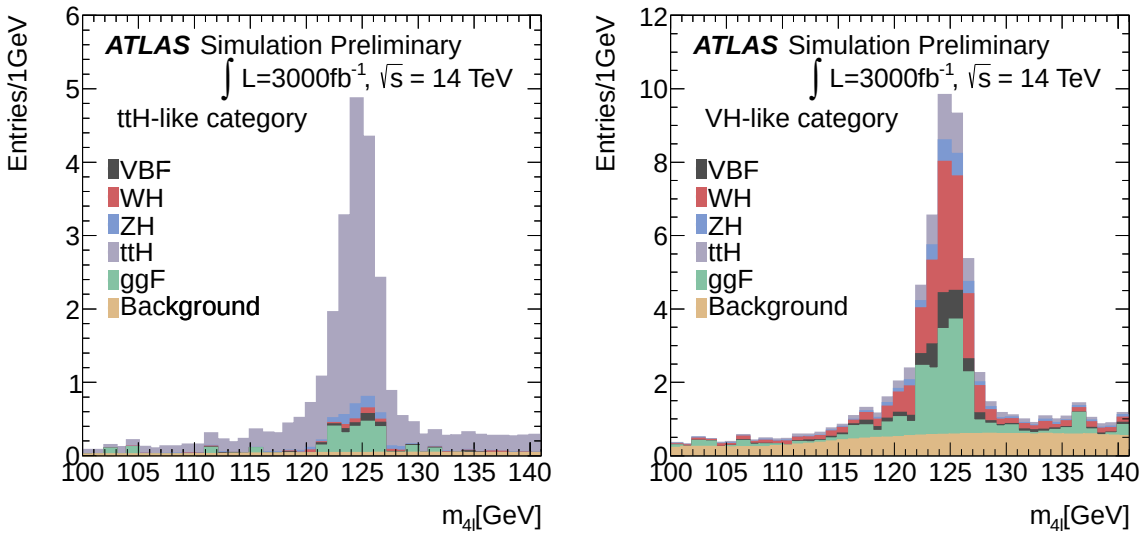

(a)

(b)

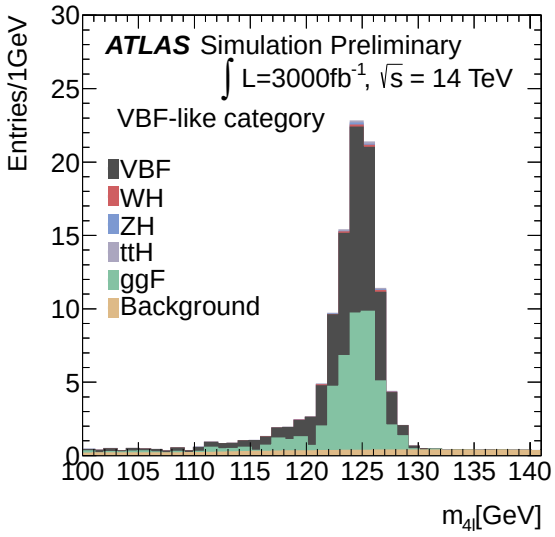

(c)

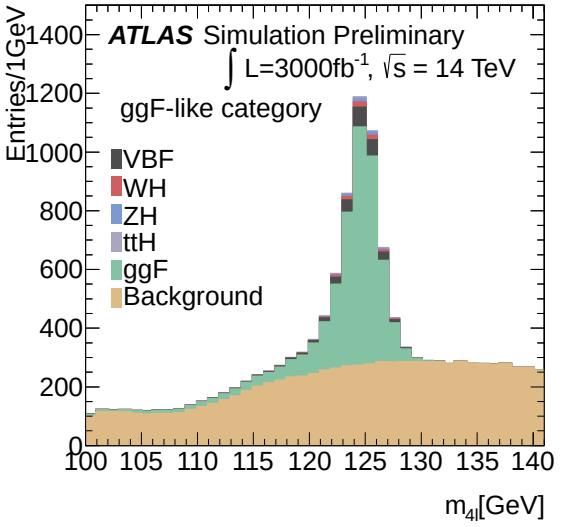

(d)

Figure 3: Invariant mass distribution of the 4-lepton system for the $t\bar{t}H$-like (a), VH-like (b), VBF-like (c) and ggF-like categories (d).

3 $H \to \gamma\gamma$

The $H \to \gamma\gamma$ channel offers a clear final state signature even in the challenging environment of the HL-LHC. With a large number of signal events in a 3000 fb^{-1} sample, this potentially allows all Higgs production modes to be studied with the same final state, which is very important for a measurement of Higgs coupling parameters.

3.1 Diphoton event selection

The selection of diphoton events follows closely the inclusive selection developed for the $H \to \gamma\gamma$ search and observation in ATLAS at 8 TeV [10]:

- two isolated photons,
- one photon with p_T>40 GeV and the other with p_T>30 GeV,
- both photons within $|\eta|$ <2.37 and outside the transition region 1.37 < $|\eta|$ < 1.52.

Simulated events with a 125 GeV Higgs boson are used as signal samples in the gluon-gluon and vector boson fusion production channels. A sample of direct diphoton events is used to study the irreducible background. Photon-jet and jet-jet samples are used for the reducible background analysis.

The available statistics are still not sufficient to model the background diphoton mass distribution expected with 3000 fb^{-1}. The background distrubution is therefore derived from an exponential fit to the available background samples, which is then used to generate high statistics pseudo-data with the expected statistical fluctuations. Figure 4 shows the diphoton spectrum of background plus signal events after $H \to \gamma\gamma$ reconstruction.

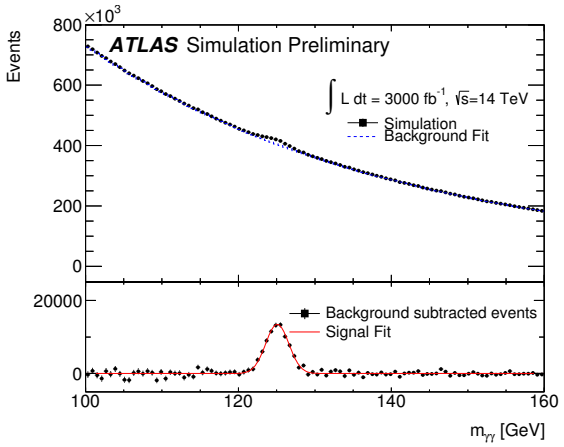

Figure 4: The expected diphoton mass distribution for the inclusive category. The blue line shows the fitted background distribution. The lower plot shows the signal distribution, fitted to the simulated signal events and pseudo-data background distribution, after subtracting the fitted background.

After combining all the generated signal and background samples, and applying the parametrised photon reconstruction performance, the invariant mass distribution is found to agree with that of previous studies for 14 TeV [1, 11].

3.2 Inclusive, 0-jet, 1-jet and 2-jet/VBF categories

Events are categorised according to the number of jets present in the event in addition to the two photons. The η dependent jet p_{T} threshold defined in section 2 is applied which gives a fake jet rate of at most 1% with $\mu_{\mathrm{pu}} = 140$. The following selection categories are then defined.

inclusive all pre-selected events.

0-jet events in which no jets are present in the event.

1-jet events with exactly one jet present in addition to the two photons.

2-jet/VBF events with exactly two jets present in addition to the two photons. Additional requirements are applied on the difference in pseudorapity of the two jets $\Delta\eta = |\eta_1 - \eta_2|$ and on the mass of the jet pair m_{jj}, as described below.

The 0-jet category has the lowest fraction of VBF events, and the 2-jet/VBF category the highest. The selection for the 3000 fb^{-1} scenario requires $\Delta\eta > 4$ and $m_{jj} > 400$ GeV. For 300 fb^{-1} scenario, these cuts are relaxed to increase the signal yield at the expense of lowering the VBF signal purity, requiring $\Delta\eta > 3$ and $m_{jj} > 300$ GeV. Figure 5 shows the distribution of $\Delta\eta$ and m_{jj} for gluon-gluon fusion and VBF signal samples, and for diphoton background events, selected by requiring two photons and two additional jets.

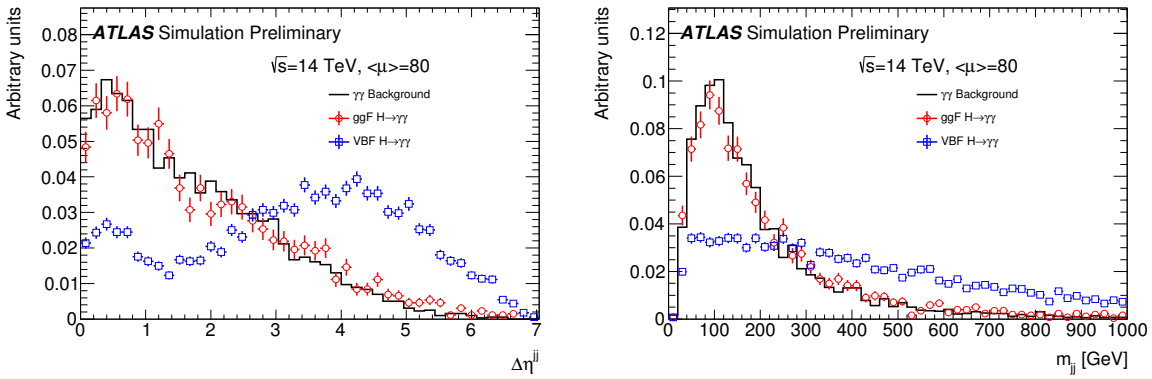

(a) (b)

Figure 5: Distribution of $\Delta\eta$ and m_{jj} in the 2-jet/VBF category.

The simulated diphoton mass distributions for events in the 0-jet, 1-jet and 2-jet/VBF categories are shown in Figure 6. Table 3 shows the number of signal and background events in the mass window 122 GeV$< m_{\gamma\gamma} <$ 128 GeV, the signal to background ratio and the fractional contribution of VBF to the signal at 14 TeV for integrated luminosities of 300 fb^{-1} and 3000 fb^{-1}. Compared to previous results [1], there are lower signal yields and higher backgrounds due to a more realistic photon identification performance.

3.2.1 Background parametrisation systematic uncertainty

The high statistics background pseudo-data are taken from an exponential distribution. The systematic uncertainty on this background modelling is estimated as the difference in the number of background events under the signal peak when fitting the background with an order-4 Bernstein polynomial and a 6-degree polynomial.

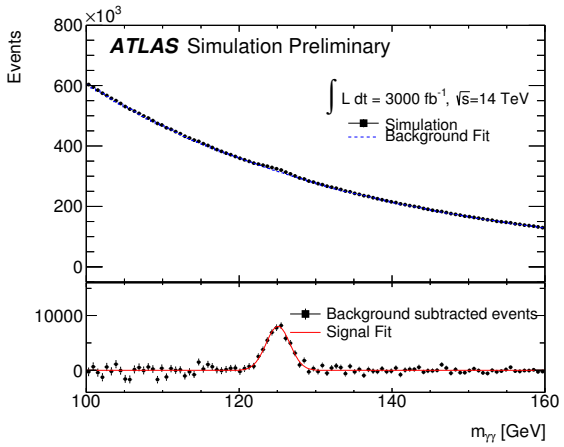

(a) Events with zero jets

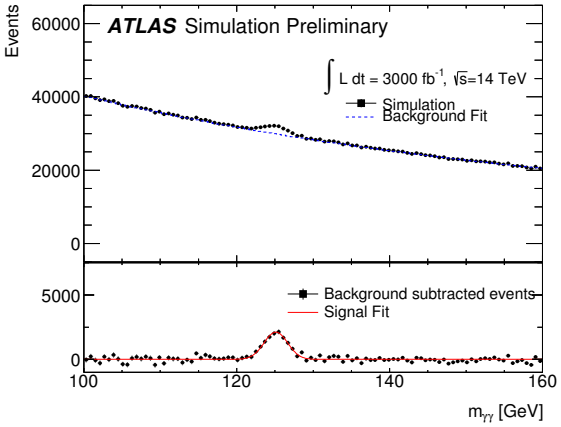

(b) Events with one jet

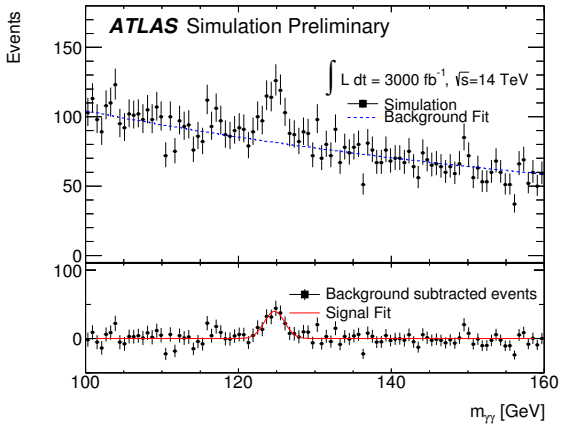

(c) Events with two jets

Figure 6: Diphoton mass spectrum for signal and both reducible and irreducible backgrounds after parametrised photon reconstruction in the 0-jet (a) 1-jet (b) and 2-jet/VBF (c) categories.

Category	Inclusive	0-jet	1-jet	2-jet
300 fb^{-1}				
S	$8.08 \cdot 10^3$	$4.92 \cdot 10^3$	$1.25 \cdot 10^3$	36.2
B	$4.06 \cdot 10^5$	$3.16 \cdot 10^5$	$3.00 \cdot 10^4$	202.7
S/B (%)	1.99	1.55	4.16	17.8
VBF/(VBF+ggF)	0.07	0.03	0.14	0.60
3000 fb^{-1}				
S	$8.08 \cdot 10^4$	$4.92 \cdot 10^4$	$1.25 \cdot 10^4$	$2.13 \cdot 10^2$
B	$4.06 \cdot 10^6$	$3.16 \cdot 10^6$	$3.00 \cdot 10^5$	$8.02 \cdot 10^2$
S/B (%)	1.99	1.55	4.16	26.56
VBF/(VBF+ggF)	0.07	0.03	0.14	0.70

Table 3: Summary of number of signal and background events in each category, ratio of signal to background and fractional contribution of VBF events to the signal with 300 fb^{-1} and 3000 fb^{-1}

Table 4 shows the common systematic uncertainty on the background parametrisation for both luminosity scenarios, 300 fb^{-1} and 3000 fb^{-1}. No difference between these two integrated luminosity scenarios is obtained in the background parametrisation systematic uncertainty.

Category	Inclusive	0-jet	1-jet	2-jet
Background uncertainty	0.017 %	0.011 %	0.037 %	0.18 %

Table 4: Systematic uncertainty on the background modelling.

3.3 Associated production of $t\bar{t}H$, WH and ZH with $H \to \gamma\gamma$

These channels have a low signal rate at the LHC, but more than 100 signal events could be observed with 3000 fb^{-1} at the HL-LHC, as reported in the study available at the time of the Update of the European Strategy for particle physics [1]. The selection of the diphoton system is done in the same way as for the inclusive $H \to \gamma\gamma$ channel. In addition, 1- and 2-lepton selections, dilepton mass cuts and different jet requirements are used to separate the WH, ZH and $t\bar{t}H$ initial states from each other and from the background processes. The $t\bar{t}H$ initial state gives the cleanest signal with a signal-to-background ratio of ~20%, to be compared to ~10% for ZH and ~2% for WH. Further improvements are envisaged, for example by optimising jet selection thresholds, or using b-tagging to separate the channels. However, these studies are still ongoing, and the previous results are retained for the coupling fits presented here.

4 $H \to Z\gamma$

The $H \to Z\gamma$ channel is interesting because the Standard Model Higgs boson can only decay via charged particle loops to this final state. However, this channel suffers from a large background from Z boson radiative production and decay. With the full Run I data collected by the ATLAS detector, the expected limit is 13.5 times the Standard Model rate [12]. The high luminosity data will be very important to be able to measure this channel in future.

4.1 $Z\gamma$ event selection

The event selection follows closely the inclusive selection developed for the $H \to Z\gamma$ search in ATLAS:

- Event triggered by a single lepton trigger with p_{T} >25 GeV or a dilepton trigger with p_{T} >20 GeV.
- One isolated photon with E_T >15 GeV, within $|\eta|$ <2.37 and not in the transition region 1.37 < $|\eta|$ < 1.52.
- Two isolated, same flavour, opposite sign electrons or muons, where electrons have p_{T} >10 GeV and $|\eta|$ <2.47, and muons have p_{T} >10 GeV and $|\eta|$ <2.7.
- The lepton pair mass satisfies m_{ll} >81.18 GeV.
- The difference $m_{ll\gamma} - m_{ll}$ between the invariant masses of the dilepton plus photon system, and the lepton pair, is used as the discriminating variable, with an expected value of around 35 GeV.

Simulated events with a 125 GeV Higgs boson are used as signal samples in the gluon-gluon and vector boson fusion production modes. The dominant background is from Z boson events with a radiative photon, and this process is also simulated. The other important background is a Z boson plus a jet which fakes a photon, which counts for 17% of the selected events in the Run 1 data. However, a dedicated

sample is not generated because it has very similar mass distributions to those of the Z boson with a true photon in the region of interest.

The available statistics are sufficient to describe the shape of the background mass distributions with 3000 fb^{-1} of data, so these are taken directly from the simulation. The background yields are normalized to the measured rate in 8 TeV data scaled by the cross section ratio, $\sigma_{14\text{TeV}}/\sigma_{8\text{TeV}} = 1.82$. Figure 7 shows the $m_{ll\gamma}$ and $m_{ll\gamma} - m_{ll}$ distributions of background events and signal events scaled to 20 times Standard Model expectation. Figure 8 shows the background with the expected signal superimposed, and the signal after background subtraction.

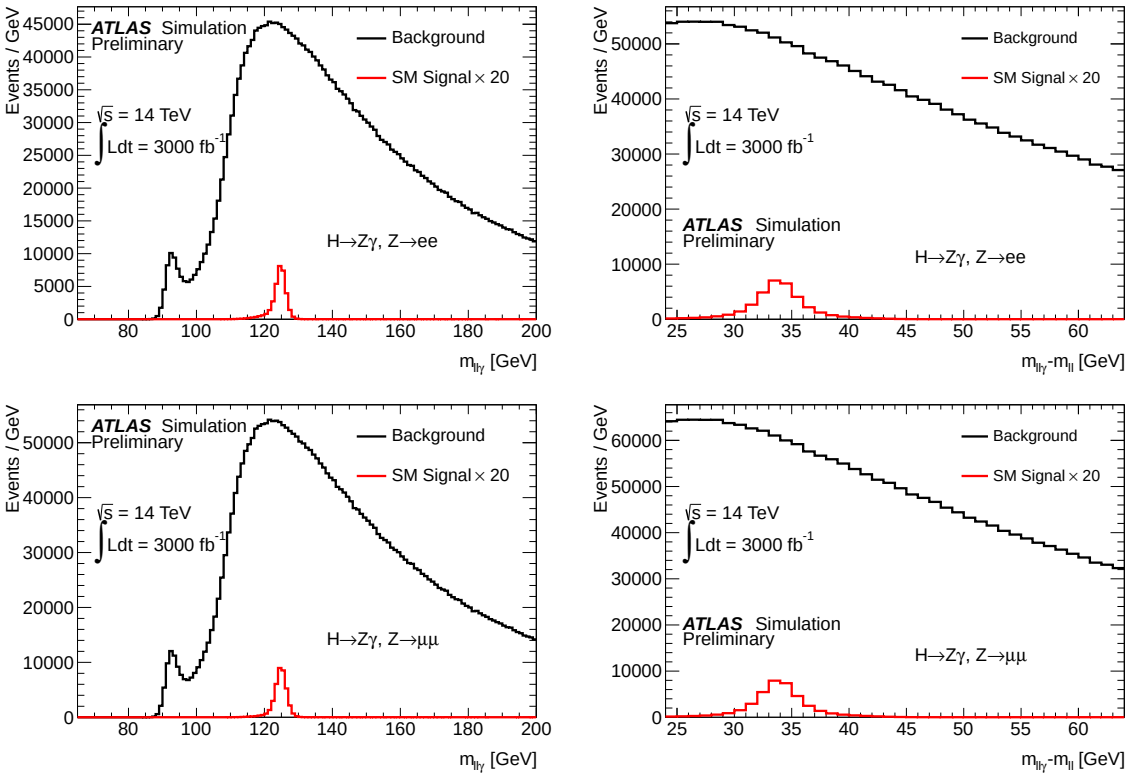

Figure 7: Distributions of $m_{ll\gamma}$ and $m_{ll\gamma} - m_{ll}$ for signal(×20) and background for the inclusive analysis.

4.2 Two jet/VBF channel

To enhance the signal to background ratio, a dedicated VBF channel search is performed by selecting two forward jets in addition. The η dependent p_{T} requirement defined in Section 2 is applied as to give a fake jet rate of $< 1\%$ with $\mu_{\text{pu}} = 140$. The difference in pseudorapidity between the two jets, $\Delta\eta$, is required to be greater than 2.8, the mass of the jet pair is required to be $m_{jj} > 400$ GeV, and the difference in azimuthal angle between the dijet system and the Higgs boson candidate, $\Delta\phi$=$|\phi_{jj} - \phi_{ll\gamma}|$ is required to be greater than 2.6. Figure 9 shows the distribution of the variables $\Delta\eta$, $\Delta\phi$ and m_{jj} in gluon-gluon fusion and VBF signal events and $Z\gamma$ background events.

4.2.1 Background parametrisation systematic uncertainty

The systematic uncertainty on the parametrisation of the background is estimated as the difference in the number of background events under the signal peak when fitting the background with a 3rd, 4th or 5th

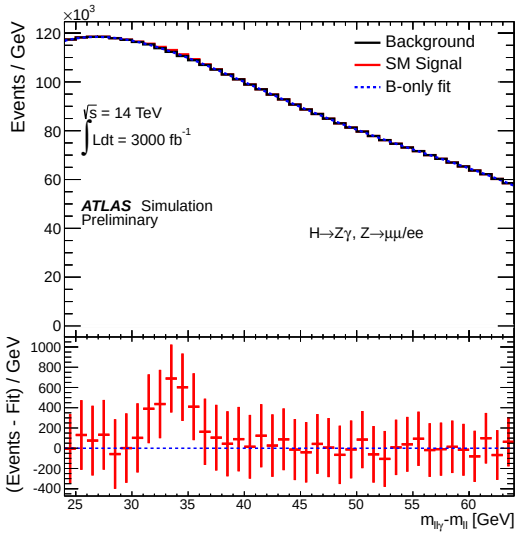

Figure 8: Distribution of $m_{ll\gamma} - m_{ll}$ for signal and background. The lower panel shows the signal after background subtraction for the inclusive analysis, with the expected data uncertainties.

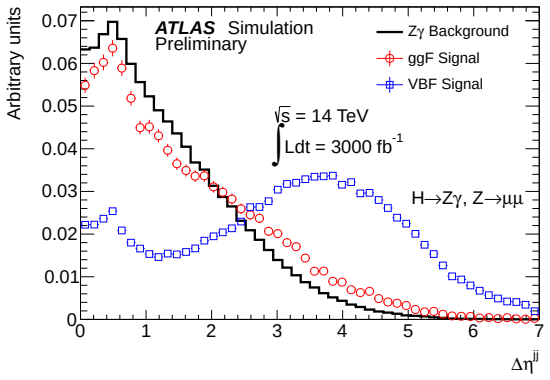

(a)

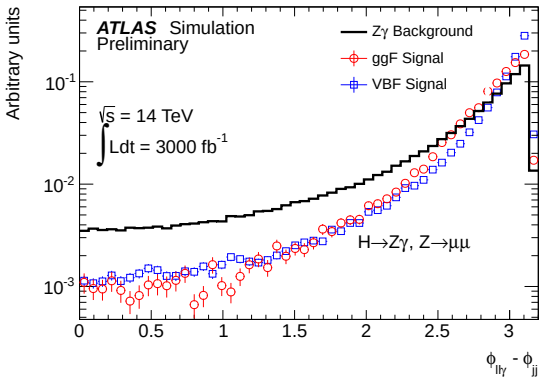

(b)

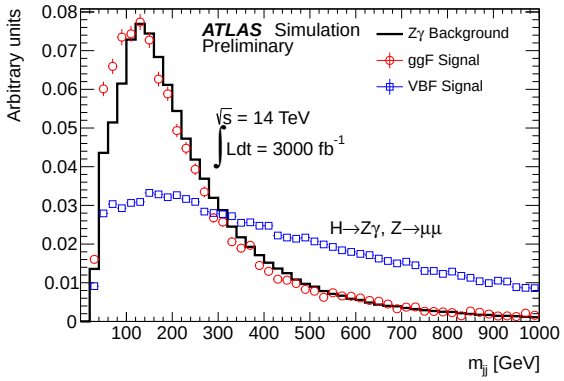

(c)

Figure 9: Distribution of $\Delta\eta$, $\Delta\phi$ and the mass of two jets present in the event.

order Bernstein or Chebychev polynomial. Table 5 shows the systematic uncertainty in the background parametrisation for 300 fb^{-1}. To be conservative, the same uncertainties are taken for the 3000 fb^{-1} case.

Channel	$ee\gamma$ inclusive	$\mu\mu\gamma$ inclusive	$ee\gamma$ VBF	$\mu\mu\gamma$ VBF
Background uncertainty	0.12 %	0.12 %	0.30 %	0.30 %

Table 5: Systematic uncertainty on the background parametrisation

4.3 Results

Table 6 shows the number of signal and background events in the range 30 GeV< $m_{ll\gamma} - m_{ll}$ <38 GeV, the signal to background ratio and the fractional contribution of VBF events to the signal at 14 TeV for 3000 fb^{-1} of integrated luminosity. Table 7 shows the expected limit and p_0 for m_H=125 GeV, for the inclusive and VBF searches with 300 and 3000 fb^{-1}.

Channel	$ee\gamma$ inclusive	$\mu\mu\gamma$ inclusive	$ee\gamma$ VBF	$\mu\mu\gamma$ VBF
S	1465	1667	21.5	23.2
B	$4.05 \cdot 10^5$	$4.84 \cdot 10^5$	609	726
S/B (%)	0.36	0.35	3.5	3.3
VBF/(VBF+ggF)	0.09	0.09	0.55	0.55

Table 6: Summary of number of signal and background events in each channel, ratio of signal over background ratios and fraction of VBF events in signal with 3000 fb^{-1}

Senario	Inclusive, 300 fb^{-1}	Inclusive, 3000 fb^{-1}	VBF, 300 fb^{-1}	VBF, 3000 fb^{-1}
Expected CLs limit (×SM)	2.53	0.74	8.12	2.50
Signal strength (σ)	0.67	2.12	0.24	0.76

Table 7: Expected CLs limit and signal strength for m_H=125GeV with inclusive and VBF searches.

5 Measuring the total width through interference

The natural width of the Higgs boson is an important physics property that could reveal new physics in case of disagreement between the prediction and the measured values. Direct measurements of the Higgs widths are not possible, as the experimental mass resolution is significantly larger than the expected width. The mass resolution of $\gamma\gamma$ systems is about 1.7 GeV for $m_{\gamma\gamma} \approx 125$ GeV, 400 times larger than the natural width. Measurements of coupling strengths paired with limits on the invisible branching fraction indirectly constrain the width to close to its SM value [13], but this strategy cannot take into account unobserved (but not truly invisible) decay modes.

5.1 Higgs boson width through interference

A new method introduced by Dixon, Li, and Martin [6,7], allows to extract an indirect limit on the Higgs width using the interference of the Higgs to diphoton signal with respect to the continuum diphoton background ($gg \to \gamma\gamma$ box diagrams). This interference has two parts.

1. An imaginary component reduces the total signal yield by 2-3%. Because this effect is degenerate with the coupling (signal strength) measurements, it is only measurable using constraints on the production rates from other channels.

2. The real component is odd around the Higgs boson mass, and does not change the yield. However, when folded with the experimental resolution, it engenders a negative shift in the apparent mass (see Figure 10).

In the SM, this shift was originally estimated using a simplified resolution model to be approximately 80 MeV [6], and for a width 20 times larger than the SM value, the shift was estimated to approximately 400 MeV. In this analysis, which use a more sophisticated resolution model and slightly adjusted selection, the shifts come out a bit smaller (about 50 MeV for the SM). The size of this shift decreases at large transverse momentum of the Higgs boson decay system, which means that the total Higgs boson width is reflected in the difference in the apparent masses between events with low and high p_{T}^{H}. This analysis relies on this feature and splits the dataset by p_{T}^{H}, at 30 GeV, and separately measures the mass difference between these two subsets. A limit on the Higgs widths is then extracted from the measured mass difference.

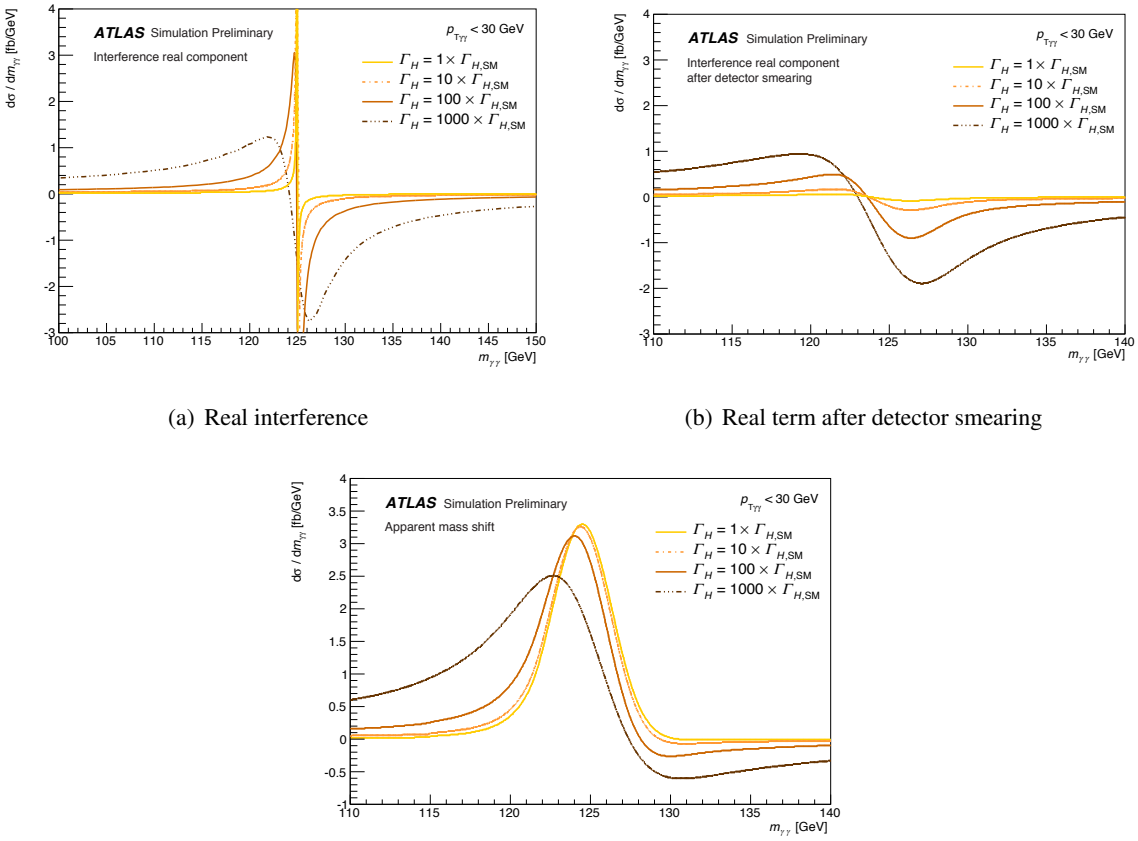

(a) Real interference

(b) Real term after detector smearing

(c) Apparent mass shift

Figure 10: The real component of the interference (a) is odd around the Higgs boson mass, with a sharp spike but long tails. Smearing this shape with the experimental resolution broadens observed cross section (b), and adding this to the nominal signal model (c) leads to a shift in the apparent mass. The interference and signal line shapes were provided by Dixon and Li, the experimental $m_{\gamma\gamma}$ resolution corresponds to the Run I resolution.

5.2 Selection

This sensitivity study follows the assumptions made in the common $H \to \gamma\gamma$ projections for 300 fb^{-1} of LHC data, and 3000 fb^{-1} of HL-LHC. The degradation of the photon identification efficiency and rejection are applied simply by appropriate scalings of the signal and background samples, as described in Section 3 and shown in Table 3. The selection follows the recent analysis of differential cross sections in $H \to \gamma\gamma$ [14]. Two isolated photons fulfilling the "tight" particle identification criterion are selected and required to be within the the detector acceptance of $|\eta| < 2.37$ and the leading (subleading) photon must have $p_{\mathrm{T}}^{\gamma}/m^{\gamma\gamma} > 0.35$ (0.25). The diphoton invariant mass is constructed from these photons.

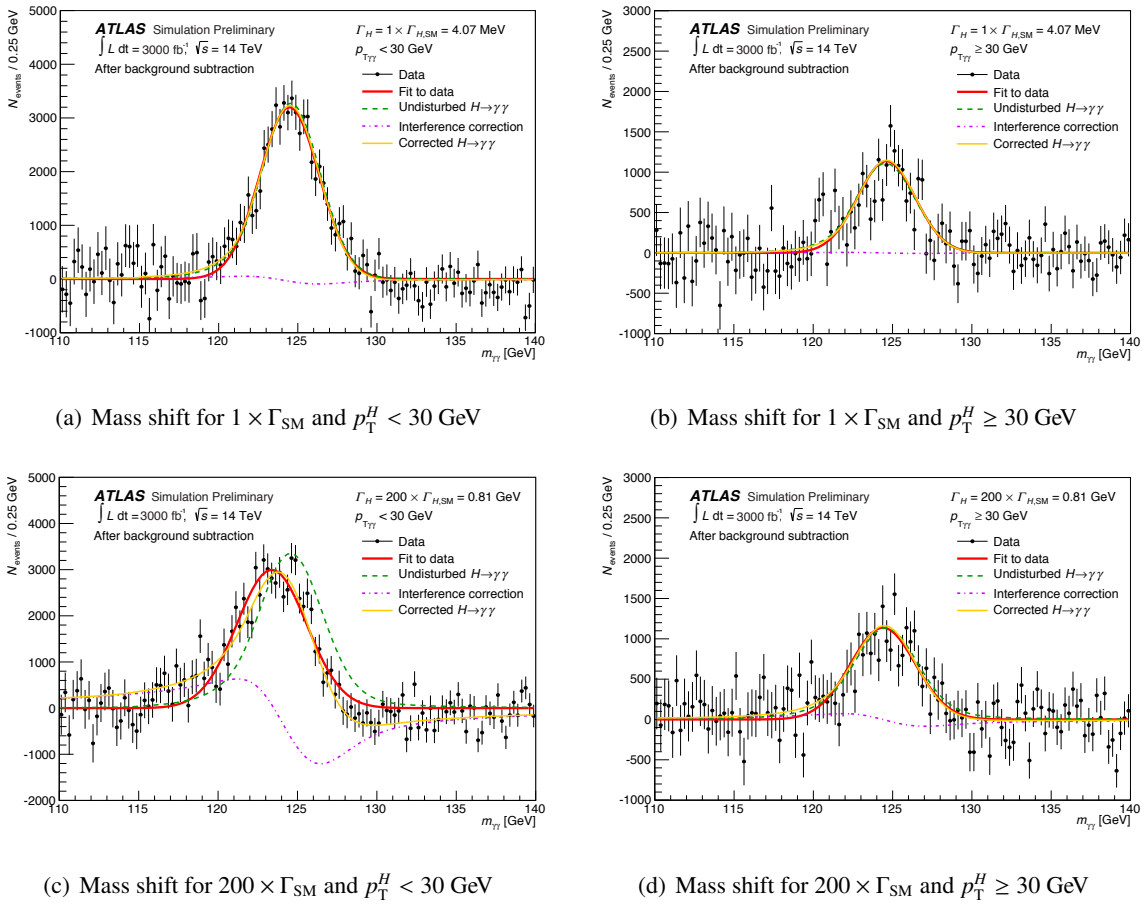

(a) Mass shift for $1 \times \Gamma_{\mathrm{SM}}$ and $p_{\mathrm{T}}^{H} < 30$ GeV

(b) Mass shift for $1 \times \Gamma_{\mathrm{SM}}$ and $p_{\mathrm{T}}^{H} \geq 30$ GeV

(c) Mass shift for $200 \times \Gamma_{\mathrm{SM}}$ and $p_{\mathrm{T}}^{H} < 30$ GeV

(d) Mass shift for $200 \times \Gamma_{\mathrm{SM}}$ and $p_{\mathrm{T}}^{H} \geq 30$ GeV

Figure 11: The mass distributions for the low- and high-p_{T}^{H} regions for $1 \times \Gamma_{\mathrm{SM}}$ and $200 \times \Gamma_{\mathrm{SM}}$ after background subtraction are illustrated: the data points correspond to a randomized sample of 3000 fb^{-1}, the green dashed line corresponds to the BW without any interference, the magenta line shows the interference correction, and the solid yellow line the summed signal and interference contribution. The red curve is a fit with a Gaussian signal PDF to illustrate the apparent mass shift.

5.3 Systematic uncertainties

This measurement benefits from extremely small systematic uncertainties as most of them, such as the dominant photon energy scale (PES) uncertainty, are correlated between the subsets and hence cancel to a very large degree when taking the mass difference. In the low-p_{T}^{H} sample, the leading and trailing photons balance, so their momenta are fairly similar. At high-p_{T}^{H}, the leading photon tends to be of

the order of 10 GeV more-boosted than at low-p_{T}^{H}, while the subleading photon is about 10 GeV less-boosted. As slightly different photon p_{T} regions are probed, non-linearities in the calorimeter response could in principle introduce some further decorrelation between the systematic uncertainties of both p_{T} regions. The impact of such a decorrelation on the limit projection is studied, by introduction an additional photon energy scale (PES) uncertainty, with a magnitude of 20% of the total PES systematics. The background modeling uncertainty (aka spurious signal) is also taken as fully uncorrelated between the two subsets. The total systematic uncertainty on the mass difference is estimated to be less than 100 MeV, which is significantly smaller than the statistical uncertainty. This analysis will benefit from the high statistics available at HL-LHC.

5.4 Projected limits

Next-to-leading order theoretical predictions that account for the interference are used for the mass line shape at nine widths ranging from $1 \times \Gamma_{\mathrm{SM}}$ to $1000 \times \Gamma_{\mathrm{SM}}$. These predictions are folded with the ATLAS Run I $m_{\gamma\gamma}$ resolution model determined separately for the low- and high-p_{T}^{H} samples, to derive the expected shifts in the apparent mass. Figure 11 shows how the mass distribution changes due to the inference for the the low and high-p_{T}^{H} regions for the $1 \times \Gamma_{\mathrm{SM}}$ and $200 \times \Gamma_{\mathrm{SM}}$ after background subtraction. Pseudo-data are then produced by folding a Breit-Wigner of the appropriate width with the resolution model, and then applying the shifts described above. For values of $\Gamma/\Gamma_{\mathrm{SM}}$ which lie between the nine widths for which a theoretical prediction is available, the predicted shift due to interference is extrapolated between existing points. The background shapes are taken from Run I data.

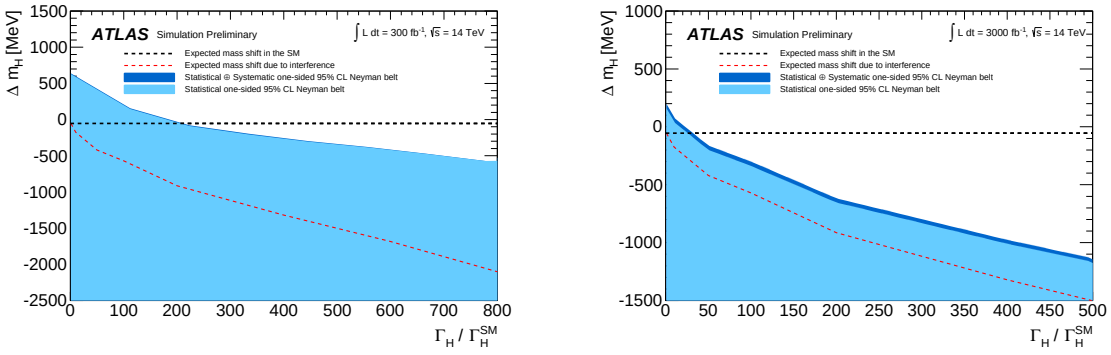

(a) 300 fb^{-1} (b) 3000 fb^{-1}

Figure 12: Projected 95% upper limits on the Higgs boson width, at 300 fb^{-1} and 3000 fb^{-1}. The dashed red line depicts the expected shift between the low- and high-p_{T} samples as a function of the true width. The black dashed line at $\Delta m_H = -54.4$ MeV is the expected shift for the SM width. The light/dark shaded region denotes allowed 95% one-sided Neyman confidence belt determined via Asimov data sets taking into account statistical (light) or statistical and systematic (dark) uncertainties. The intercepts between the SM value and the blue curves are the expected upper limits on the width, assuming a SM Higgs boson.

These data are used to derive 95% CL upper limits on the Higgs boson width, as shown in Fig. 12. If the Higgs boson has SM width, an expected limit may be set at $220 \times \Gamma_{\mathrm{SM}} \approx 880$ MeV with 300 fb^{-1} of data, or $40 \times \Gamma_{\mathrm{SM}} \approx 160$ MeV with 3000 fb^{-1}. Introducing an additional uncorrelated PES component to account for unexpected non-linearity effects, reduce the expected sensitivity to $230 \times \Gamma_{\mathrm{SM}} \approx 920$ MeV

with 300 fb^{-1} of data, or $50 \times \Gamma_{\rm SM} \approx 200$ MeV with 3000 fb^{-1}. The expected total (statistical) uncertainty on the mass difference assuming a SM width are 420 MeV (410 MeV) for 300 fb^{-1} and 170 MeV (130 MeV) for 3000 fb^{-1}. The obtained limits may be compared to the current, direct 95% limit from CMS, of 6.9 GeV, using 2011 and 2012 data [15].

5.5 Further Work

Reoptimization of the photon identification to maintain the photon/jet discrimination is critical for this statistics-limited analysis. An obvious, but incorrect development of the analysis, would be to use more than two $p_{\rm T}^H$ bins. Theoretical uncertainties do not allow for multiple splits below 30 GeV, and above 30 GeV the shift is flat and nearly zero.

Below the Higgs peak, the interference produces a simple enhancement in the diphoton spectrum; above the Higgs peak, it produces a deficit. Together, these create an offset between the "plateau" regions above and below the resonance peak in the $m_{\gamma\gamma}$ spectrum. This is visible in Figure 10. A possible extension to the work presented would be to use not only the shift in the measured peak, but also this offset when evaluating the interference.

6 $H \to WW$

This section documents the study of the $H \to WW \to \ell\nu\ell\nu$ channel, where $\ell = e, \mu$. It differs from most of the other analyses presented in this note, because it is based on reconstructed events with 8 TeV centre-of-mass energy, rather than generator level 14 TeV samples.

6.1 Simulation tools

The analysis presented here uses detector level reconstructed events in 8 TeV Monte Carlo samples which are extrapolated to the 14 TeV conditions by parton distribution function (PDF) reweighting and emulation of the difference in performance of the ATLAS detector in the high pile-up environment. The standard smearing functions serve as the baseline for simulating the experimental effects on physics objects in the case of event pile-up levels of $\mu_{\rm pu} = 50$ and $\mu_{\rm pu} = 140$, but in this case they are applied to reconstructed objects in the 8 TeV samples. Additional studies were performed, such as the evaluation of the loss in the trigger efficiency in the higher pile-up conditions, application of the necessary additional jet $p_{\rm T}$ smearing, the $p_{\rm T}$ and η distributions of pile-up jets, the evaluation of the degradation of the resolution of the soft terms in the track-$E_{\rm T}^{\rm miss}$ and a check of the stability of the 85% efficient b-tagging working point with the higher level of pile-up.

6.2 Analysis

Higgs boson production is studied in the gluon-gluon fusion (ggF) and vector boson fusion (VBF) modes, considering final states with 0, 1 or ≥ 2 jets. The Higgs boson mass is assumed to be 125 GeV. This section describes the object and event selection, systematic uncertainties and the final event yields used to extract the signal strength.

The background processes studied include the irreducible SM WW production, $t\bar{t}$ and single top ($tW/tb/tqb$), non-WW diboson ($W\gamma/WZ/ZZ$, so-called VV), Z/γ+jets and W+jets processes. The event yields are normalised to the cross sections predicted at $\sqrt{s} = 14$ TeV when they have been explicitly computed. Otherwise they are normalised to the $\sqrt{s} = 8$ TeV cross sections and scaled by the ratios of cross sections of similar processes.

6.2.1 Object and event selection

The object and event selection follows closely the selection used for the latest Run 1 results [16]. Electrons and muons are required to be isolated and have $p_{\mathrm{T}} > 15$ GeV. The lepton identification, reconstruction and isolation efficiency is kept at the same level as for the current 8 TeV analysis. More refined identification techniques will compensate the degradation of the detector performance. To cope with the higher level of pile-up, the jet p_{T} threshold was raised to 30 (35) GeV in the central and forward regions in the case of $\mu_{\mathrm{pu}} = 50$ (140). The requirement of a track confirmation (here extended to 80 GeV in the central region) allows jets to be selected with a p_{T} threshold as low as 30 GeV at an affordable fake rate [5]. The residual contribution from pile-up jets has been taken into account in the simulation using their predicted p_{T} and η spectra. Events with only two oppositely charged and different flavour ($e\mu + \mu e$) leptons passing a set of quality cuts are selected. The leading lepton is required to have a p_{T} greater than 25 GeV and the cut on the minimum invariant mass of the leptons, $m_{\ell\ell}$, is 10 GeV. The Drell-Yan and multi-jet backgrounds are suppressed with a cut on the jet-corrected track-$E_{\mathrm{T}}^{\mathrm{miss}}$. The track-based $E_{\mathrm{T}}^{\mathrm{miss}}$ is calculated from the tracks associated to the primary vertex and passing a set of quality cuts. In addition, lepton tracks that failed the quality criteria are also added to the computation. An update to the track-$E_{\mathrm{T}}^{\mathrm{miss}}$ calculation relies on correcting it for neutral particles in analysis jets by replacing the tracks associated with jets with the calibrated jet p_{T} (jet-corrected track-$E_{\mathrm{T}}^{\mathrm{miss}}$). This variant of $E_{\mathrm{T}}^{\mathrm{miss}}$ was found to be the most stable against pile-up and it additionally improves the scale, resolution and direction with respect to the true $E_{\mathrm{T}}^{\mathrm{miss}}$ in the events with jets.

To profit from the different background rates and compositions, the analysis is split according to the number of jets, N_{jet}, present in the events. The $N_{\mathrm{jet}} = 0$ and $= 1$ channels are sensitive to ggF production and $N_{\mathrm{jet}} \geq 2$ to VBF production. The $N_{\mathrm{jet}} \geq 2$ selection is optimised to reduce the effects of the higher pile-up conditions. The jet p_{T} threshold was raised to 45 GeV, and the jets are required to be in opposite hemispheres with $|\eta_{\mathrm{jet}}| > 2.0$. A veto is placed on additional central jets above 30 GeV. A requirement of $m_{\mathrm{jj}} > 1.25$ TeV is made to significantly reduce the contamination from $t\bar{t}$ background. For future optimisation, a fit to the dijet mass, m_{jj}, or to the $p_{\mathrm{T}}^{\mathrm{jet}}$ distributions could be performed to further discriminate between the signal and the backgrounds, and to reduce the uncertainties. At present, a fit is made to the transverse mass, m_{T}, distribution to extract the sensitivity to the presence of the Higgs boson. Final event yields with the corresponding systematic uncertainties are summarised in the following section.

6.2.2 Systematic uncertainties and results

The dominant experimental systematic uncertainties (jet energy scale and resolution, and the b-tagging efficiency) are expected to be smaller with the increased data statistics. Background modelling will be significantly improved thanks to the available statistics in the control regions. Additional control regions (same sign lepton selection or signal region side bands) will help in understanding the leading backgrounds and reducing the uncertainties. The current 8 TeV theoretical uncertainties on the signal processes are used. They are shown in Table 8. A summary of the total systematic uncertainties per background process, and per N_{jet} bin, is given Table 9. A comparison to the previous upgrade study done for the European Strategy meeting and to the current 8 TeV uncertainties is presented. Any MC-statistics-related uncertainty is neglected for the extraction of the precision on the signal strength measurement.

Tables 10 and 11 show the final event yields at the stage where the fit to the m_{T} distribution is performed. The large increase of the event yields with 3000 fb^{-1} in the $N_{\mathrm{jet}} \geq 2$ channel with respect to 300 fb^{-1}, is caused by the higher pile-up conditions, where the $E_{\mathrm{T}}^{\mathrm{miss}}$ and jet energy resolutions are degraded and the rate of jets from pile-up interactions is increased.

A similar sensitivity study has been performed for the European Strategy meeting and is documented here [1]. Compared to the previous study, the jet p_{T} threshold has been raised; consequently, the rate in the $N_{\mathrm{jet}} = 0$ channel increased by ~25-30%. The efficiency of the m_{T} window cut, which could be

	$N_{\text{jet}} = 0$	$N_{\text{jet}} = 1$	$N_{\text{jet}} \geq 2$
ggF QCD scale	17	37	43
ggF QCD acceptance	4	4	4
ggF PDF	8	8	8
ggF UE/PS	3	10	9
ggF total	19	39	44
VBF QCD scale	1	1	1
VBF QCD acceptance	4	4	4
VBF PDF	3	3	3
VBF UE/PS	3	10	3
VBF total	6	11	6

Table 8: Current theoretical uncertainties (in %) for the 8 TeV analysis. The uncertainties are split into the QCD scale and acceptance uncertainties, PDF and UE/PS uncertainties.

	$N_{\text{jet}} = 0$			$N_{\text{jet}} = 1$			$N_{\text{jet}} \geq 2$		
	14 TeV	ES	8 TeV	14 TeV	ES	8 TeV	14 TeV	ES	8 TeV
WW	1.5	5	5	5	-	6.5	10	10	30
VV	2	15	15	5	-	20	10	20	20
$t\bar{t}$	7	7	12	8	-	23	10	15	33
$tW/tb/tqb$	7	7	12	8	-	23	10	15	33
Z+jets	10	10	15	10	-	18	10	10	20
W+jets	20	30	30	20	-	30	20	100	30

Table 9: The total systematic uncertainty (in %) for the background processes. The uncertainties used in the last upgrade study are shown in the columns labelled "ES". The uncertainties used in the latest public 8 TeV results are also quoted. The $N_{\text{jet}} = 1$ channel was not considered in the previous analysis.

placed to select a region with the optimal significance, also increased from ~20% to ~60% in the $N_{\text{jet}} = 0$ channel. This efficiency is directly linked to the m_{T} resolution and it shows the improvement coming from using the track-$E_{\text{T}}^{\text{miss}}$ and not the default calorimeter-based one.

The expected precision on the signal strength measurement has been obtained by fitting the m_{T} distribution. The distributions used are shown in Figures 13, 14 and 15. The different background uncertainties are assumed to be uncorrelated between different jet multiplicity bins and a 3% luminosity uncertainty has been added. The uncertainty on the $H \rightarrow WW$ branching ratio is also included. The results, for the two scenarios of the pile-up and integrated luminosity levels, are shown in Table 12. They combine the $N_{\text{jet}} = 0$, $= 1$ and ≥ 2 final states. The precision of the signal strength, $\Delta\mu/\mu$, is found to be $O(10\%)$ with 3000 fb^{-1}. The previous upgrade study reported $\Delta\mu/\mu$ of $O(25\%)$. The assumptions on the systematic uncertainties and the optimisation of the $N_{\text{jet}} \geq 2$ channel, are the key differences between the previous upgrade study and the analysis presented in this note. The inclusion of the $N_{\text{jet}} = 1$ channel also contributed to improving the precision on the signal strength, but to a lesser extent than the previously mentioned updates.

N_{jet}	N_{bkg}	N_{signal}	N_{ggF}	N_{VBF}	N_{WW}	N_{VV}	$N_{t\bar{t}}$	N_t	$N_{\text{Z+jets}}$	$N_{\text{W+jets}}$
$= 0$	34330	4380	4300	80	19000	3500	6000	2600	370	2860
$= 1$	21460	1970	1740	230	5760	1800	9360	2850	710	980
≥ 2	101	62	5	57	12	4	60	5	12	8

Table 10: The signal and background event yields as expected at 14 TeV, with $\mu_{\text{pu}} = 50$ and 300 fb^{-1}, and before the m_{T} requirement. The signal is split based on the production mode of the Higgs boson.

N_{jet}	N_{bkg}	N_{signal}	N_{ggF}	N_{VBF}	N_{WW}	N_{VV}	$N_{t\bar{t}}$	N_t	$N_{\text{Z+jets}}$	$N_{\text{W+jets}}$
$= 0$	366450	41840	40850	990	172950	32000	96600	32150	4150	28600
$= 1$	259610	22375	20050	2325	68810	21570	119560	28110	11200	10360
≥ 2	1825	590	90	500	300	120	745	245	335	80

Table 11: The signal and background event yields as expected at 14 TeV, with $\mu_{\text{pu}} = 140$ and 3000 fb^{-1}, and before the m_{T} requirement. The signal is split based on the production mode of the Higgs boson.

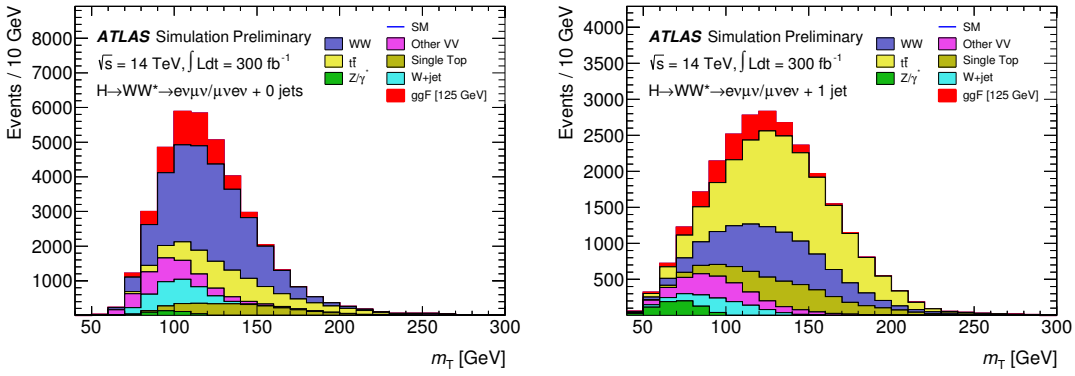

Figure 13: The m_{T} distributions after all the selection cuts, but before the final m_{T} window cut, in the $N_{\text{jet}} = 0$ (left) and $N_{\text{jet}} = 1$ (right) final states for $\mu_{\text{pu}} = 50$ with 300 fb^{-1} of total integrated luminosity.

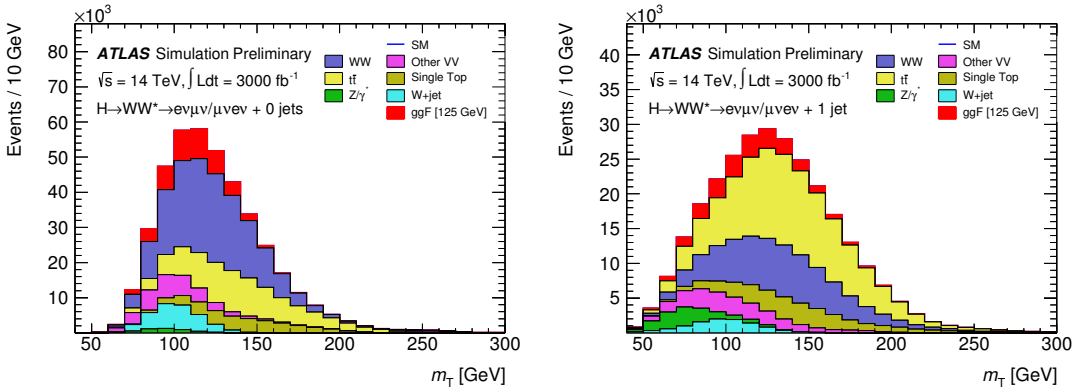

Figure 14: The m_{T} distributions after all the selection cuts, but before the final m_{T} window cut, in the $N_{\mathrm{jet}} = 0$ (left) and $N_{\mathrm{jet}} = 1$ (right) final states for $\mu_{\mathrm{pu}} = 140$ with 3000 fb^{-1} of total integrated luminosity.

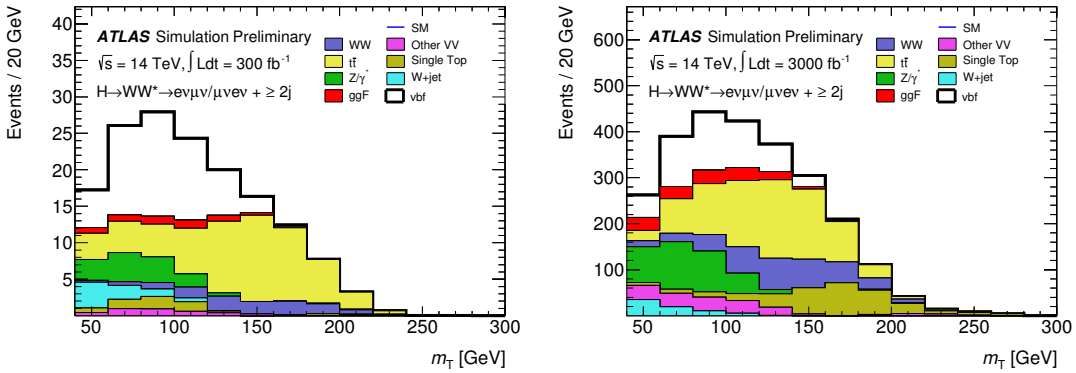

Figure 15: The m_{T} distribution after all the selection cuts, but before the final m_{T} cut, in the $N_{\mathrm{jet}} \geq 2$ final state for $\mu_{\mathrm{pu}} = 50$ with 300 fb^{-1} of total integrated luminosity (left) and $\mu_{\mathrm{pu}} = 140$ with 3000 fb^{-1} of total integrated luminosity (right) .

	μ_{ggF}	μ_{VBF}	$\mu_{\mathrm{ggF+VBF}}$
300 fb^{-1}	$1^{+0.18}_{-0.15}$	$1^{+0.25}_{-0.22}$	$1^{+0.14}_{-0.13}$
3000 fb^{-1}	$1^{+0.16}_{-0.14}$	$1^{+0.15}_{-0.15}$	$1^{+0.10}_{-0.09}$

Table 12: The precison on the signal strength measurement for $\mu_{\mathrm{pu}} = 50$ and 140, and for different Higgs production modes. $N_{\mathrm{jet}} = 0$, $= 1$ and ≥ 2 final states are combined.

7 $H \to \tau\tau$

The $H \to \tau\tau$ results presented here are those that were available at the time of the input to the European Strategy update [1]. Further studies have been made to investigate the sensitivity of the results to including more backgrounds in addition to the dominant $Z \to \tau\tau$, and to updating the $E_{\mathrm{T}}^{\mathrm{miss}}$ modelling in particular for the 300 fb^{-1} (where the performance based on Run 1 with $\mu_{\mathrm{pu}} = 10$ was assumed). The selection cuts were reoptimised, which more than compensated for the additional background for the $\mu_{\mathrm{pu}} = 140$ sample. Since the changes to the sensitivity were small compared to the anticipated gain from a more sophisticated analysis, and including all channels, the previous results are retained at this stage.

Only VBF Higgs production is considered, and in the modes where both τ leptons decay to an electron or muon and neutrinos (di-lepton) or one τ decays leptonically and the other hadronically. This does not exploit the full potential of $\tau\tau$ final states; based on Run-1 experience it is already established that boosted categories and the VH channels also make a significant contribution.

7.1 VBF $H \to \tau\tau \to \ell^+\ell^- 4\nu$

The leptonic τ decays are easier to trigger on, but the di-lepton final state has a lower branching ratio than the lepton-hadron state. A comparison was made with a 7 TeV sample of the results of applying the selection criteria on full simulation, and the output of the parametrised performance applied to generator level. Good agreement at the level of a few per cent was found.

The signal and main backgrounds at 14 TeV are estimated for 300 and 3000 fb^{-1}. The event selection requires two opposite sign leptons with $p_{\mathrm{T}} > 25$ (35) GeV for 300 (3000) fb^{-1}, at least two jets with a central jet veto and a b-jet veto, and $E_{\mathrm{T}}^{\mathrm{miss}} > 40$ (20) GeV for same flavour (opposite flavour) lepton pairs. After all cuts, the expected number of signal events is 55 (147) for 300 (3000) fb^{-1} with 56 (190) background events.

7.2 VBF $H \to \tau\tau \to \ell\tau_{had} 3\nu$

Although the mixed leptonic-hadronic decay channel has a higher branching ratio than the di-lepton channel, it is very challenging. Many improvements have been made in the hadronic τ identification and Higgs mass estimation algorithms since the time of the analysis on which this extrapolation is based. A comparison of parametrised and full simulation results at 7 TeV is again used to validate the method. The selection at 14 TeV results in 145 (297) signal and 628 (1610) background events for 300 (3000) fb^{-1}.

7.3 Extrapolation of lower energy $\tau\tau$ results to 300 fb^{-1} at 14 TeV

In order to estimate the full potential identifying the $H \to \tau\tau$ signal over the large background affecting this final state, a combination of dedicated analyses is needed targetting production modes such as VBF, boosted and non-boosted gluon-gluon processes, associated VH and ttH production mechanisms, for each distinct final state obtainable from the di-tau system. From 7 and 8 TeV analysis, we expect the total sensitivity of be roughly a factor of two more precise than a measurement using the VBF channels alone, as illustrated below.

Going from 8 TeV to 14 TeV, the signal Higgs cross-section for a boson mass of 125 GeV increases by a factor 2.6, while that of the dominant Drell-Yan $Z \to \tau\tau$ background increases by a factor 1.8. This means that $S/\sqrt{B}$ increases by a factor of 1.9. However, challenging effects from increased pile-up conditions and higher trigger thresholds may degrade the sensitivity by roughly a similar factor. Therefore, we perform an extrapolation of the cut-based analysis at 7 and 8 TeV with $\sim$10 fb^{-1} up to 14 TeV and 300 fb^{-1}. without taking advantage of this extra 1.9 factor.

We assume that, while the statistical error on the signal and background events scale with luminosity, the systematic uncertainties include constant terms due to theoretical uncertainties and to the background level uncertainties. The contribution due to theory uncertainties is 9%, while the experimental uncertainty is at the level of 7 %, yielding an overall systematic uncertainty of about 11 %.

The extrapolation of the signal sensitivity using the two statistically independent data samples at 7 and 8 TeV respectively, gives a signal significance of 6.9 σ, i.e. a 15 % uncertainty in the signal strength.

In this note, these extrapolated results are included to illustrate the range of predictions under different assumptions. For the Higgs coupling fits the more conservative cut-based analysis results are retained.

8 $H \to \mu\mu$

The sensitivity of ATLAS to the rare process $H \to \mu^+\mu^-$ is studied for the benchmark mass point of $m_H = 125$ GeV. This channel allows the coupling to second generation fermions to be probed, and can contribute to mass measurements due to the high resolution of the reconstructed $\mu^+\mu^-$ invariant mass. Searches in this channel are challenged by the low branching fraction of the $H \to \mu^+\mu^-$ decay and high contributions of background processes such as Z/γ^* production. The analysis is based on the search for neutral MSSM Higgs bosons in the $\mu^+\mu^-$ channel [17] performed on the 2011 data set and the 2012 SM $H \to \mu^+\mu^-$ search [18] while minimal changes are made to optimise the analysis.

This note is an update of the analysis already presented for the European Strategy [1, 2] adding the signal contribution from the VBF, VH and ttH production modes to the inclusive analysis and switching to the signal and background parametrisation from the 2012 SM $H \to \mu^+\mu^-$ search. The analysis still uses the old smearing functions [4], so the result does not take advantage of the improved resolution with the Phase-II inner tracker [3]. The previous dedicated ttH analysis is retained in addition to the inclusive search.

8.1 Monte Carlo Samples

The signal process $gg \to H \to \mu^+\mu^-$ is simulated, and the yield is then scaled up to account for the other production modes. For the background the three dominant processes are taken into account. These are the production of Z/γ^* in association with jets, and the production of $t\bar{t}$ and WW pairs.

8.2 Event Selection

The following selection criteria are applied to the generated and corrected signal and background events. The single high-p_T muon trigger decision is emulated by requiring at least one muon with $p_T > 25$ GeV and $|\eta| < 2.4$. In addition, at least one muon with a p_T of greater than 20 GeV and $|\eta| < 2.5$ is required. The muon tracks are required to be isolated. Since pile-up events are not simulated, the track-based isolation is taken into account by applying the measured efficiency in full simulation. After applying this efficiency correction, full and parametrised simulation agree at the level of 4% in a Run 1 sample.

A $\mu^+\mu^-$ pair is chosen from the two highest p_T muons having opposite charge. Because of a generator cut on the Z/γ^* data sets $\mu^+\mu^-$ pairs with an invariant mass $m_{\mu^+\mu^-} > 70$ GeV are selected.

The resulting $\mu^+\mu^-$ invariant mass distribution of the signal and background processes are shown in Figure 16 for an integrated luminosity of 3000 fb^{-1}. Even for invariant masses well beyond the Z resonance the Z/γ^* production dominates the background in this analysis. In the mass range $m_{\mu^+\mu^-} > 110$ GeV its relative fraction amounts to 80.6 %, while $t\bar{t}$ and WW productions contribute with 19.3 % and 0.1 %, respectively.

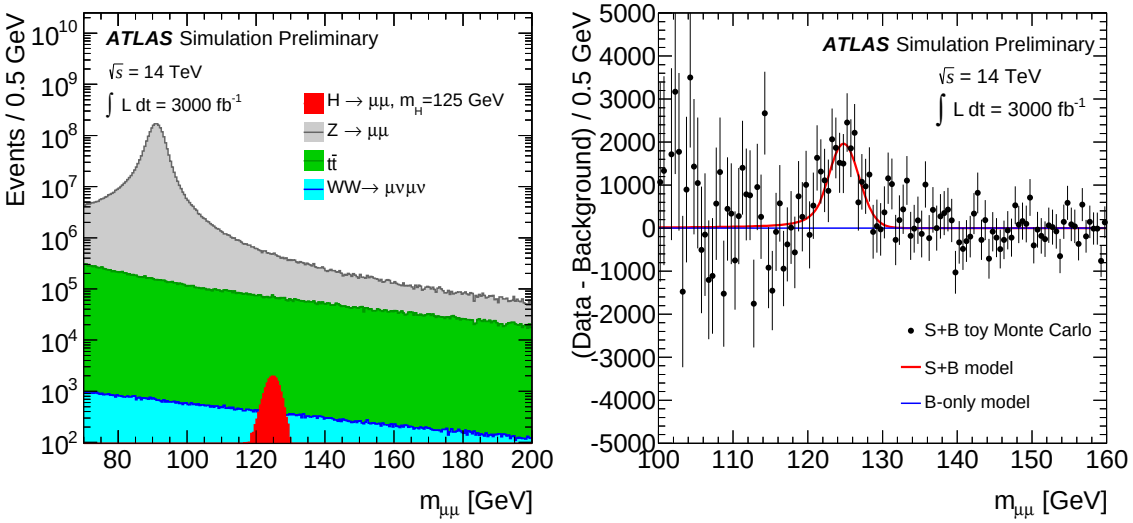

(a) (b)

Figure 16: (a) Distribution of the $\mu^+\mu^-$ invariant mass of the signal and background processes generated for $\sqrt{s} = 14\,\text{TeV}$ and $\mathcal{L} = 3000\,\text{fb}^{-1}$. (b) Background subtracted invariant mass distribution of a toy MC sample generated under the signal-plus-background hypothesis for $\mathcal{L} = 3000\,\text{fb}^{-1}$.

8.3 Signal and Background Modelling

The final discriminating variable in the $H \to \mu^+\mu^-$ searches is the $\mu^+\mu^-$ invariant mass distribution. The shape and normalisation of the total background is estimated from data by fitting the signal and background parametrisation introduced in Ref. [18] to the invariant mass distribution.

A binned likelihood fit of the total $\mu^+\mu^-$ invariant mass distribution is performed in the mass range of 100 GeV to 160 GeV to estimate the free parameters of the background model. The resulting fit parameters define the background estimate. Uncertainties on the shape and normalisation of the background estimate are obtained from the fit uncertainties of the individual model parameters. A negligible systematic uncertainty in the background model is assessed by using alternative functions, either an exponential together with a 4th order Bernstein polynomial, or the model from the 2011 MSSM $h/A/H \to \mu^+\mu^-$.

Figure 16 (b) shows the estimated background subtracted from a toy MC sample generated from the signal-plus-background hypothesis expected for an integrated luminosity of $3000\,\text{fb}^{-1}$. For comparison the tested signal-plus-background and background only hypotheses are shown as well.

8.4 Results

The resulting number of signal and background events in a mass range of 122 GeV to 128 GeV are shown in Table 13 for the two scenarios with $\sqrt{s} = 14$ TeV and $300\,\text{fb}^{-1}$ or $3000\,\text{fb}^{-1}$, respectively. The uncertainty from the background estimation of the fit is shown. The expected signal significance and the precision on the combined signal strength μ are obtained from the complete distributions in the full fit range of 100 GeV to 160 GeV taking into account the signal and background shapes. With an integrated luminosity of $3000\,\text{fb}^{-1}$, the $H \to \mu^+\mu^-$ channel can be observed, with an expected significance of 7.0σ.

$\mathcal{L}$ [fb^{-1}]	300	3000
N_{ggH}	1510	15100
N_{VBF}	125	1250
N_{WH}	45	450
N_{ZH}	27	270
N_{ttH}	18	180
N_{Bkg}	564000	5640000
$\Delta^{\mathrm{sys}}_{Bkg}$ (model)	68	110
$\Delta^{\mathrm{sys}}_{Bkg}$ (fit)	190	620
$\Delta^{\mathrm{stat}}_{\mathrm{S+B}}$	750	2380
Signal significance	2.3σ	7.0σ
$\Delta\mu/\mu$	46%	21%

Table 13: Numbers of expected signal and background events in a mass window of ±3 GeV around the $m_H = 125$ GeV benchmark point for the HL-LHC scenarios. The uncertainty from the background estimation of the fit is shown. The signal significance and the precision on the combined signal strength μ are obtained accounting for the full shape information using the invariant mass distributions in a mass range of 100 GeV to 160 GeV.

8.5 $ttH, H \to \mu\mu$

A study of this rare channel has two motivations. First, it allows a direct measurement of the product of the top- and the μ-Yukawa coupling, neither of which are accessible through the standard Higgs channels. Second, this channel could be valuable for the determination of the CP nature of the resonance at 125 GeV. The CP odd component could be supressed with a vector boson coupling in the initial or final state, but there are only fermion Yukawa couplings in this channel. The result has not been updated from the inputs to the European Strategy discussion [1].

The method chosen follows the a1, a2, b1-b4 CP variable definitions [19]. Signal samples with CP even (H) or CP odd (A) Higgs bosons are generated using Madgraph5 and Pythia 8. The events must have at least two muons with opposite charge and $p_{\mathrm{T}} > 35$ GeV, no more than four leptons, at least 4 jets and a Higgs candidate mass, formed from the two muons, between 120 and 130 GeV. The distribution of the di-muon mass is shown in Fig. 17. The expected number of events after all the selections is 33 for signal and 22 for background, allowing this channel to be observed with the HL-LHC.

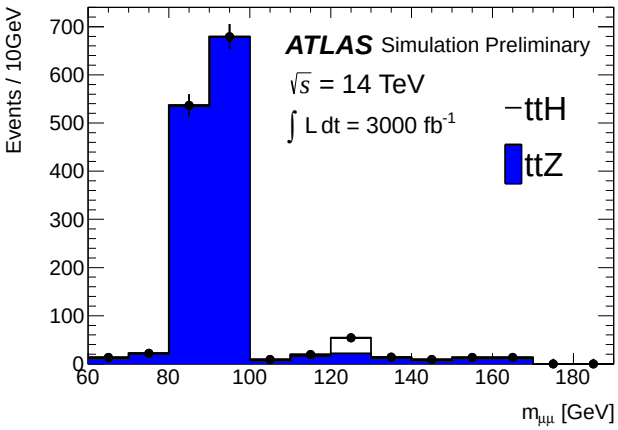

Figure 17: The invariant mass of the di-muon system in the ttH, $H \to \mu\mu$ channel.

9 Search for ZH with $H \to$ invisible final states

The channel $ZH \to \ell^+\ell^-+$ invisible offers the possibility of searching directly for the invisible branching fraction of the Higgs boson [20]. This approach is complementary to the indirect constraint from the Higgs coupling measurements.

9.1 Event Selection

Electrons and muons are required to have p_{T} larger than 20 GeV. A looser threshold of 7 GeV is considered for the third lepton veto to suppress the WZ background. Electrons (muons) are required to have $|\eta| < 2.47(2.5)$. Jets are required to have $p_{\mathrm{T}} > 30$ GeV for $|\eta| < 2.1$, and $p_{\mathrm{T}} > 50$ GeV for $2.1 \leq |\eta| < 2.5$. These thresholds are expected to result in a jet fake rate from the pileup of 10% for $\langle\mu\rangle = 140$. After the selection of electrons, muons and jets, overlap removal is imposed among these objects. Jets are removed when they are within $\Delta R = 0.2$ of a selected electron. Electrons are removed if they are within $\Delta R = 0.2$ of an identified muon. Finally, remaining electrons and muons are removed if they are within $\Delta R = 0.4$ of a remaining jet.

The event selection is based on the recent ATLAS Run 1 analysis [21] with some modifications. First of all, the track-based missing transverse momentum is not considered. The $E_{\mathrm{T}}^{\mathrm{miss}}$ threshold and some of the angular cuts are relaxed due to the degradation of object performance coming from the higher pile-up conditions. Table 14 summarizes the event selection adopted for this study, and Table 15 shows the expected background and signal yields for the two luminosity scenarios. Only the statistical uncertainty from the simulated samples is shown. Figure 18 shows the $E_{\mathrm{T}}^{\mathrm{miss}}$ distributions for the two scenarios. The dramatic increase in the Z+jets background at high μ_{pu} is due to the degraded $E_{\mathrm{T}}^{\mathrm{miss}}$ performance. However, the Z+jets background is concentrated in the lowest $E_{\mathrm{T}}^{\mathrm{miss}}$ bins, so the signal sensitivity remains in the higher bins. Moreover, this background could still be suppressed by adding a $d\phi(E_{\mathrm{T}}^{\mathrm{miss}}, \vec{p}_{\mathrm{T}}^{\mathrm{miss}})$ cut.

Cut variables	Thresholds
$E_{\mathrm{T}}^{\mathrm{miss}}$	> 180 GeV
$\mathrm{d}\phi(\ell, \ell)$	< 1.2
$\mathrm{d}\phi(\vec{p}_{\mathrm{T}}^{\,\ell,\ell}, \vec{E}_{\mathrm{T}}^{\mathrm{miss}})$	> 2.7
$\lvert E_{\mathrm{T}}^{\mathrm{miss}}\text{-}\ p_{\mathrm{T}}^{\ell,\ell}\rvert / p_{\mathrm{T}}^{\ell,\ell}$	< 0.6
Jet veto	> 25 GeV

Table 14: Cut thresholds optimized for the high pile-up scenarios.

Expected yields	300 fb^{-1}	3000 fb^{-1}
ZZ	1321 ± 53	12000 ± 500
WZ	440 ± 2	4501 ± 22
WW	0.9 ± 0.9	52 ± 21
Top	127 ± 37	1810 ± 440
Z+jets	172 ± 87	82000 ± 6100
Signal (125 GeV, BR($H \to$ inv.)=20%)	154 ± 2	1379 ± 21

Table 15: Background and signal yields for 300 and 3000 fb^{-1} of 14 TeV data. Only the statistical uncertainty from the MC samples is shown.

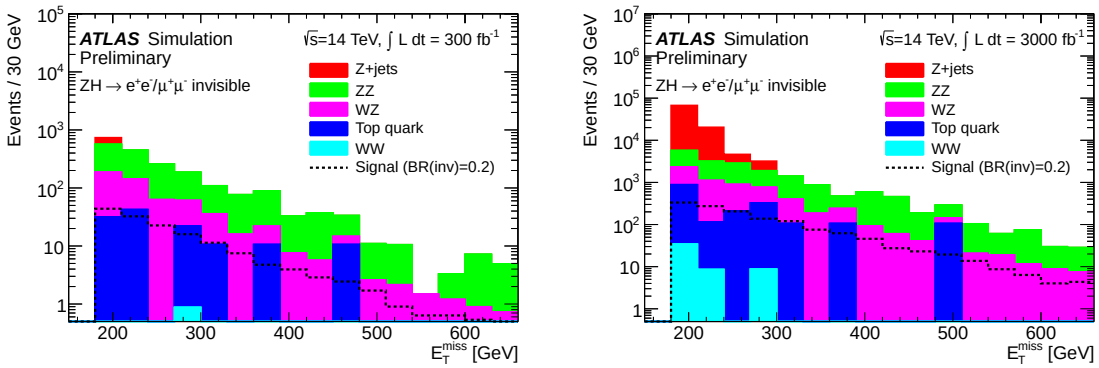

Figure 18: $E_{\mathrm{T}}^{\mathrm{miss}}$ distributions for 300 and 3000 fb^{-1} 14 TeV data samples.

9.2 Systematic uncertainties

Two scenarios are considered to predict the systematic uncertainties.

For the so-called conservative scenario, an experimental uncertainty of 5%, theoretical uncertainty of 4.7%, and jet veto systematic uncertainties of 5.5% are assumed for the ZZ and WZ backgrounds.

For the so-called realistic case, the uncertainty is expected to become smaller due to large statistics. From the expected yields of the $ZZ \to 4\ell$ and $WZ \to \ell\nu\ell\ell$, the overall uncertainty of the ZZ background is estimated to be 6.7% for 300 fb^{-1} and 2.2% for 3000 fb^{-1}. Similarly, the overall uncertainty of the WZ background is estimated to be 3.0% for 300 fb^{-1} and 1.0% for 3000 fb^{-1}.

The WW, top quark, and $Z \to \tau^+\tau^-$ backgrounds are estimated to have the overall uncertainty of 8.8% for 300 fb^{-1} and 2.3% for 3000 fb^{-1}, considering the expected event yields in the eμ control region. The Z background is assumed to have an uncertainty of 10%, but this background is expected to be suppressed significantly by the $d\phi(E_{\mathrm{T}}^{\mathrm{miss}}, \vec{p}_{\mathrm{T}}^{\mathrm{miss}})$ selection, which is not applied in this note.

For the signals, an experimental uncertainty of 4.0%, theoretical uncertainty of 5.0%, and a jet veto systematic error of 5.5% are considered for all cases.

9.3 Results

The limits are calculated with the CL_s modified frequentist formalism using a maximum likelihood fit using the $E_{\mathrm{T}}^{\mathrm{miss}}$distributions with a profile likelihood test statistics. During the limit setting, the theoretical uncertainty of the ZZ and WZ backgrounds are assumed to be fully correlated, whereas for the jet veto systematics, the correlation among the signals, ZZ and WZ backgrounds are taken into account. The uncertainty coming from the MC statistics is not considered during the limit setting, as it is expected to be significantly reduced in the future. Table 16 shows the expected limits for the two scenarios. The branching ratio of 23-32% (8-16%) is expected to be excluded at 95% confidence level with 300 fb^{-1} (3000 fb^{-1}) of data at $\sqrt{s} = 14$ TeV.

BR(H →inv.) limits at 95% (90%) CL	300 fb^{-1}	3000 fb^{-1}
Realistic scenario	23% (19%)	8.0% (6.7%)
Conservative scenario	32% (27%)	16% (13%)

Table 16: Expected limits with 95% (90%) CL on the invisible branching ratio of the Higgs boson are shown. The Standard Model cross section for ZH production is assumed.

9.4 Interpretation with Higgs-Portal Models

The invisible decay of the Higgs boson can be interpreted in the context of the dark matter particles coupling to the Higgs boson. Such dark matter models are called the Higgs-portal models [22–25].

In those models, the limits on the invisible branching fraction of the Higgs boson can thus be interpreted as the bounds on the strength of the interaction between the dark matter and the Higgs boson. We define the strength as the coupling constant, $\lambda_{h\chi\chi}$. The bounds on the coupling constant can be further mapped to the dark matter-nucleon scattering cross section, and can be compared with dark matter direct detection experiments [26–33]. The relationship between the invisible branching fraction, the coupling constant, and the dark matter-nucleon scattering cross section depend on the spin of the dark matter particle [23–25, 34]. Three spin scenarios are considered in this note: a scalar, vector, or majorana-fermion.

Figure 19 shows the 90% CL upper limits on the dark matter-nucleon scattering cross section. The ATLAS interpretation is specific to the Higgs-portal models, whereas the results from the direct detection experiments are generic. Figure 20 shows the upper limits on the Higgs-dark matter couplings.

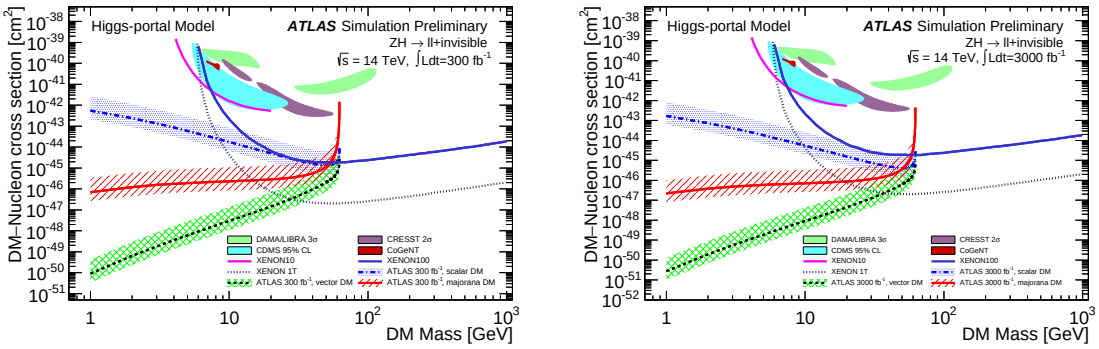

Figure 19: Upper limits (90% CL) on the dark matter-nucleon scattering cross section in Higgs-portal scenarios, extracted from the expected Higgs to invisible branching fraction limit and from direct-search experiments. The results are shown for three spin scenarios of the DM candidate: a scalar, vector or fermion particle. The hatched areas correspond to the uncertainty of the nucleon form factor.

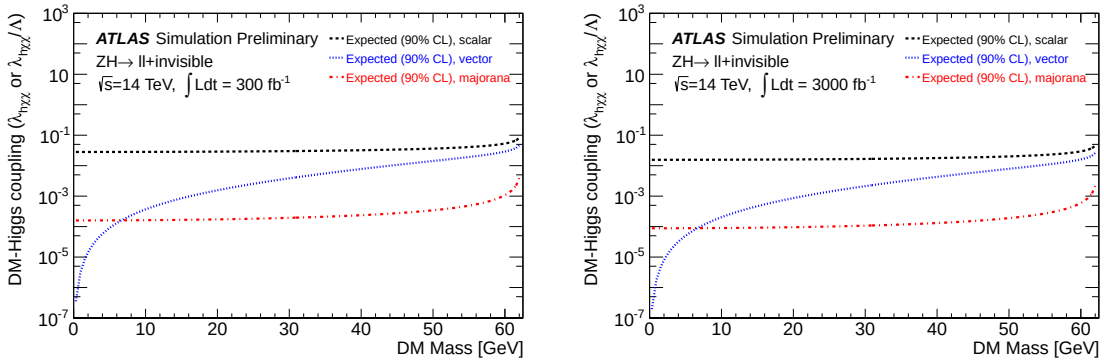

Figure 20: Limits on the Higgs-dark matter couplings in Higgs-portal scenarios, extracted from the expected Higgs to invisible branching fraction limit. The results are shown for three spin scenarios of the DM candidate: a scalar, vector or fermion particle.

10 Higgs boson pair production

An intrinsic property of the Standard Model Higgs boson is its self-coupling, the strength of which must be established in order to test whether the observed Higgs boson fulfills its crucial role in electroweak symmetry breaking. Higgs boson pair production in proton-proton collisions is characterized by the destructive interference of diagrams in which the Higgs boson is produced with and without a triple-Higgs vertex.

The dominant production mechanism at the LHC is the gluon-gluon production mode. At $\sqrt{s}$ = 14 TeV, the production cross section for a pair of 125 GeV Higgs bosons, assuming the Standard Model value for the self-coupling ($\lambda_{HHH} = 1 \times \lambda_{\mathrm{SM}}$), is estimated at NLO to be 34^{+6}_{-5}(QCDscale) ± 1(PDFs)fb. This cross section would be enhanced for values of the self-coupling lower than those predicted by the SM, while it would be strongly reduced for larger values. For example, for $\lambda_{HHH} = 0(2) \times \lambda_{\mathrm{SM}}$ the cross section is predicted to be 71 (16) fb.

Studies of di-Higgs boson production in the $bb\gamma\gamma$ and $bb\tau\tau$ final states are ongoing. The measurement of this process is very challenging, but is nevertheless anticipated to be accessible at some level at the HL-LHC.

11 Coupling fit

The results from the individual channels described in the previous sections are combined in this section to extract information about the Higgs boson couplings. The statistical treatment of the analysis is described in Refs. [35–40].

In order to obtain an overview of the relative strength of the different experimental analysis categories entering the combination, the uncertainty in the ratio of fitted total signal strength to the SM expectation assuming a Higgs boson with a mass of 125 GeV, is shown in Fig. 21 and Table 17.

11.1 Overview of common systematic uncertainties

For the signal theory uncertainties, the QCD scale, (PDF + α_S) and BR uncertainties are given in Ref. [41–43]. The BR uncertainties for the different final states are treated as uncorrelated. However, it was tested that a correlated treatment based on the uncertainties of the partial decay width [41] results in only very small differences. For the (anti-)correlated uncertainty contributions for different jet mulitplicities in the $gg \to H$ process the same numbers as for the 8 TeV analysis are used [41]. All common signal theory uncertainties are treated as 100% correlated between all channels. For the luminosity an uncertainty of 3% is assumed. Other systematic uncertainties are considered to be analysis specific and treated uncorrelated between channels.

In the following, two sets of results are presented: using the current theory uncertainties as summarized above and assuming no theory uncertainties, which is the expected experimental limit for a measurement. Intermediate assumptions on how the theory uncertainty might scale by the time 3000 fb^{-1} is reached, e.g. 50% of the current uncertainty, can be reached by quadratic interpolation between these extremes.

11.2 Definition of coupling fit framework

Following the approach recommended in Refs. [41], measurements of coupling scale factors are implemented using a leading-order tree-level motivated framework. This framework is based on the following assumptions:

$\Delta\mu/\mu$	300 fb^{-1}		3000 fb^{-1}	
	All unc.	No theory unc.	All unc.	No theory unc.
$H \to \mu\mu$ (comb.)	0.39	0.38	0.15	0.12
(incl.)	0.47	0.45	0.19	0.15
(ttH-like)	0.73	0.72	0.26	0.23
$H \to \tau\tau$ (VBF-like)	0.22	0.16	0.19	0.12
$H \to ZZ$ (comb.)	0.12	0.06	0.10	0.04
(VH-like)	0.32	0.31	0.13	0.12
(ttH-like)	0.46	0.44	0.20	0.16
(VBF-like)	0.34	0.31	0.21	0.16
(ggF-like)	0.13	0.06	0.12	0.04
$H \to WW$ (comb.)	0.13	0.08	0.09	0.05
(VBF-like)	0.21	0.20	0.12	0.09
(+1j)	0.36	0.17	0.33	0.10
(+0j)	0.20	0.08	0.19	0.05
$H \to Z\gamma$ (incl.)	1.47	1.45	0.57	0.54
$H \to \gamma\gamma$ (comb.)	0.14	0.09	0.10	0.04
(VH-like)	0.77	0.77	0.26	0.25
(ttH-like)	0.55	0.54	0.21	0.17
(VBF-like)	0.47	0.43	0.21	0.15
(+1j)	0.37	0.14	0.37	0.05
(+0j)	0.22	0.12	0.20	0.05

Table 17: Relative uncertainty on the signal strength μ for the combination of Higgs analysis at 14 TeV, 300 fb^{-1} (left) and 3000 fb^{-1} (right), assuming a SM Higgs Boson with a mass of 125 GeV. For both 300 and 3000 fb^{-1} the first column shows the results including current theory systematic uncertainties, while the second column shows the uncertainties obtained using only the statistical and experimental systematic uncertainties. The abbreviation "(comb.)" indicates that the precision on μ is obtained from the combination of the measurements from the different experimental sub-categories for the same final state, while "(incl.)" indicates that the measurement from the inclusive analysis was used.

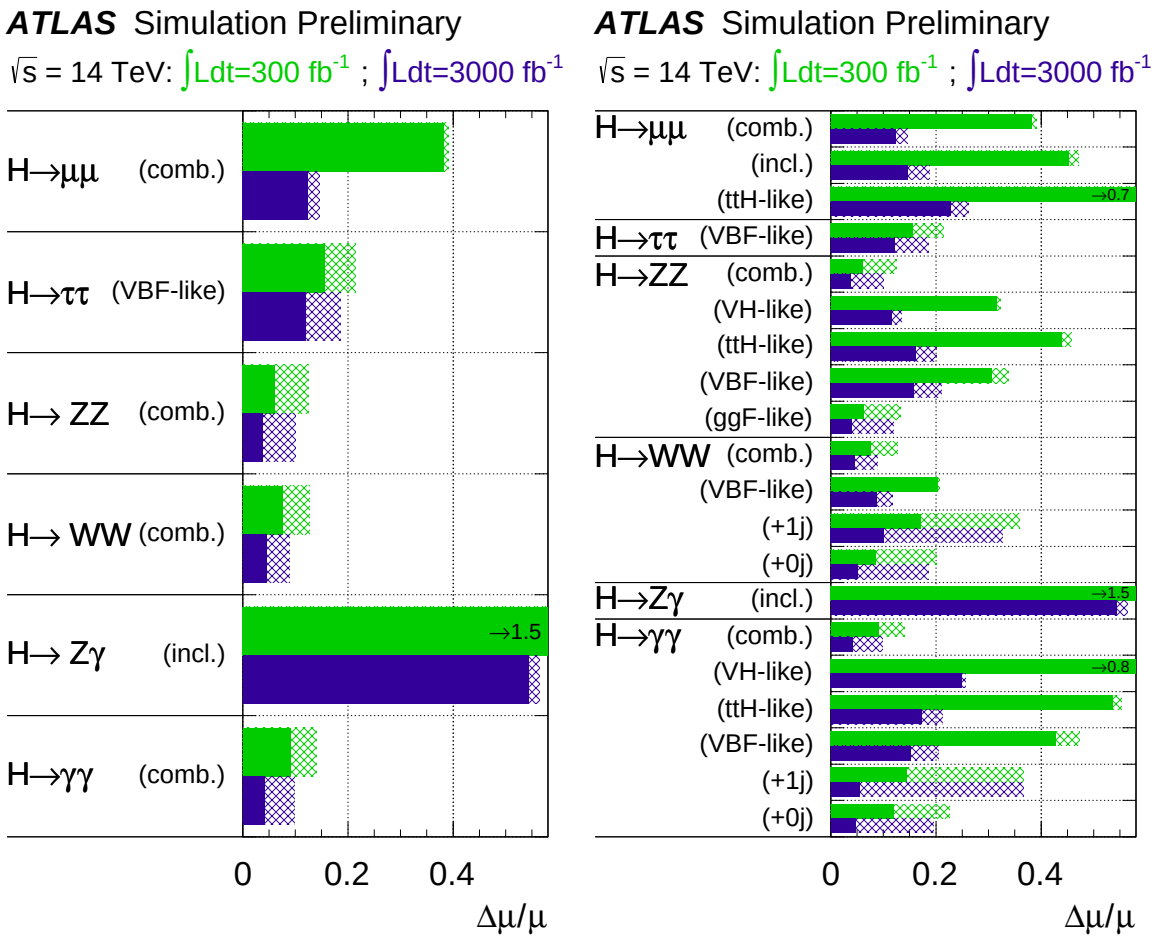

Figure 21: Relative uncertainty on the total signal strength μ for all Higgs final states in the different experimental categories used in the combination, assuming a SM Higgs Boson with a mass of 125 GeV and LHC at 14 TeV, 300 fb^{-1} and 3000 fb^{-1}. The hashed areas indicate the increase of the estimated error due to current theory systematic uncertainties. The abbreviation "(comb.)" indicates that the precision on μ is obtained from the combination of the measurements from the different experimental sub-categories for the same final state, while "(incl.)" indicates that the measurement from the inclusive analysis was used. The left side shows only the combined signal strength in the considered final states, while the right side also shows the signal strength in the main experimental sub-categories within each final state.

- The signals observed in the different search channels originate from a single resonance. A mass of 125 GeV is assumed here.
- The width of the Higgs boson is narrow, justifying the use of the zero-width approximation (this can be verified using a measurement as discussed in Section 5). Hence the predicted rate for a given channel can be decomposed in the following way:

$$\sigma \cdot B\,(i \to H \to f) = \frac{\sigma_i \cdot \Gamma_f}{\Gamma_H} \tag{1}$$

where σ_i is the production cross section through the initial state i, B and Γ_f are the branching ratio and partial decay width into the final state f, respectively, and Γ_H the total width of the Higgs

boson.

- Only modifications of coupling strengths are considered, while the tensor structure of the Lagrangian is assumed to be the same as in the Standard Model. This implies in particular that the observed state is a CP-even scalar (this can be verified using a mesurement as discussed in Ref. [44]).

The coupling scale factors κ_j are defined in such a way that the cross sections σ_j and the partial decay widths Γ_j associated with the SM particle j scale with κ_j^2 compared to the SM prediction [41]. With this notation, and with κ_H^2 being the scale factor for the total Higgs boson width Γ_H, the cross section for the $gg \to H \to \gamma\gamma$ process, for example, can be expressed as:

$$\frac{\sigma \cdot B\,(gg \to H \to \gamma\gamma)}{\sigma_{\mathrm{SM}}(gg \to H) \cdot B_{\mathrm{SM}}(H \to \gamma\gamma)} = \frac{\kappa_g^2 \cdot \kappa_\gamma^2}{\kappa_H^2} \tag{2}$$

In some of the fits, κ_H and the effective scale factors κ_γ, $\kappa_{(Z\gamma)}$ and κ_g for the loop-induced $H \to \gamma\gamma$, $H \to Z\gamma$ and $gg \to H$ processes are expressed as a function of the more fundamental factors κ_W, κ_Z, κ_t, κ_b, κ_τ and κ_μ (only the dominant fermion contributions are indicated here for simplicity). The relevant relationships are:

$$\kappa_g^2(\kappa_b, \kappa_t) = \frac{\kappa_t^2 \cdot \sigma_{ggH}^{tt} + \kappa_b^2 \cdot \sigma_{ggH}^{bb} + \kappa_t\kappa_b \cdot \sigma_{ggH}^{tb}}{\sigma_{ggH}^{tt} + \sigma_{ggH}^{bb} + \sigma_{ggH}^{tb}}$$

$$\kappa_\gamma^2(\kappa_b, \kappa_t, \kappa_\tau, \kappa_W) = \frac{\sum_{i,j} \kappa_i\kappa_j \cdot \Gamma_{\gamma\gamma}^{ij}}{\sum_{i,j} \Gamma_{\gamma\gamma}^{ij}} \tag{3}$$

$$\kappa_{(Z\gamma)}^2(\kappa_b, \kappa_t, \kappa_\tau, \kappa_W) = \frac{\sum_{i,j} \kappa_i\kappa_j \cdot \Gamma_{Z\gamma}^{ij}}{\sum_{i,j} \Gamma_{Z\gamma}^{ij}}$$

$$\kappa_H^2 = \sum_{\substack{jj=WW,\, ZZ,\, b\bar{b},\, \tau^-\tau^+,\\ \gamma\gamma,\, Z\gamma,\, gg,\, t\bar{t},\, c\bar{c},\, s\bar{s},\, \mu^-\mu^+}} \frac{\kappa_j^2 \Gamma_{jj}^{\mathrm{SM}}}{\Gamma_H^{\mathrm{SM}}}$$

where σ_{ggH}^{ij}, $\Gamma_{\gamma\gamma}^{ij}$, $\Gamma_{Z\gamma}^{ij}$ and $\Gamma_{ff}^{\mathrm{SM}}$ are obtained from theory [41]. Unless dedicated fit parameters κ_γ, $\kappa_{(Z\gamma)}$ or κ_g are assigned to these effective coupling scale factors, the relations above are used in the fits.

11.3 Coupling fit results

The Higgs boson coupling scale factors are determined from a combined fit to all channels, where the product $\sigma \cdot B\,(i \to H \to f)$ of cross section and branching ratio for all contributing Higgs signal channels is expressed as function of the coupling scale factors κ_i. Depending on the assumptions involved, different benchmark parametrizations are used following the recommendations in Ref. [41]. The benchmark parametrizations fall into two overall categories depending on assumptions on the total width: On the one hand there are those parametrizations without assumptions on the total width, which then allow only

measurements of ratios $\lambda_{ij} = \kappa_i/\kappa_j$ of coupling scale factors. On the other hand, if assumptions on the total width are made, absolute couplings κ_i can be extracted. A detailed discussion of these assumptions can be found in Ref. [41]. The expected total width measurements as outlined in Section 5 are not sufficiently precise to replace such assumptions.

Even in the absence of new decay modes, the Higgs total width can still differ from the Standard Model expectation if any of its couplings to SM particles differ from their expected values. In the absence of a dedicated $H \to bb$ extrapolation to high luminosity, the constraint on the b-coupling κ_b, which is essential for the total width, is obtained mainly from the $H \to \tau\tau$ or $H \to \mu\mu$ channel, depending on the chosen parametrizations.

The precision on a given coupling parameter is specific to the particular parametrization in which it is probed; general parametrizations with more parameters and fewer simplifying assumptions generally result in the parameters being determined with larger uncertainties.

A minimal coupling fit is shown in the parametrization with one universal coupling to vector bosons, $\kappa_V = \kappa_Z = \kappa_W$, and one universal coupling to fermions, $\kappa_F = \kappa_t = \kappa_b = \kappa_\tau = \kappa_\mu$. Such a measurement is most sensitive to deviations from the SM between the Higgs boson Gauge- and Yukawa-coupling-sector. In this parametrization, the $H \to \gamma\gamma$ and $gg \to H$ loops and the total Higgs boson width depend only on κ_F and κ_V, with no contributions from physics beyond the Standard Model (BSM). Experimental precisions of ~1.5% on κ_V and ~3% on κ_F are expected with 3000 fb^{-1} (~2.5% and ~4% with current theory uncertainties). This is a significant reduction compared to the 300 fb^{-1} expectation, which gives ~2.5% on κ_V and ~7% on κ_F (~3.5% and ~8.5% with current theory uncertainties). Detailed results are given in Figure 22 and in model Nr. 2 in Table 18.

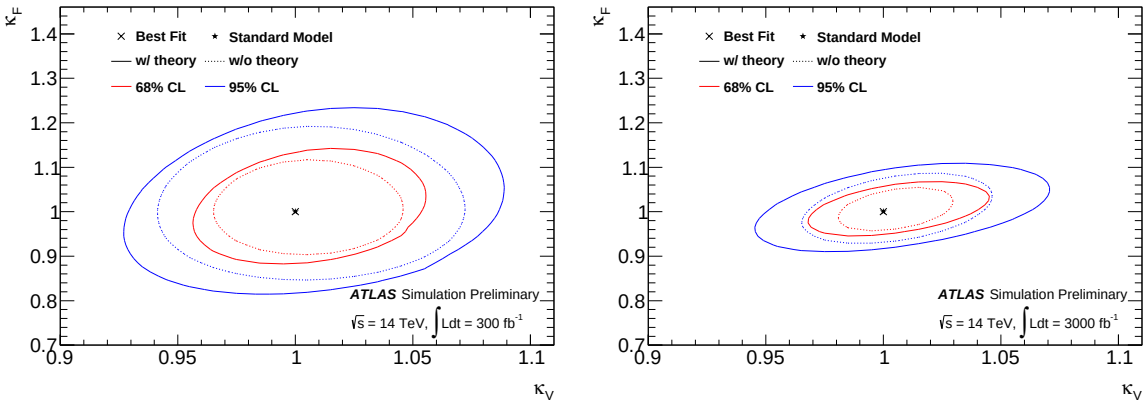

Figure 22: 68% and 95% CL likelihood contours for κ_V and κ_F in a minimal coupling fit at 14 TeV for an assumed integrated luminosity of 300 fb^{-1} (Left) and for 3000 fb^{-1} (Right).

Some extensions of this minimal coupling fit, which all assume no extra BSM Higgs decays, are shown in models Nr. 3-5 in Table 18. In model Nr. 3 the assumption on identical scaling between the different Gauge- and Yukawa-couplings is removed (with the exception of the b-coupling κ_b, as discussed above), while the assumptions on no BSM particles contributing to the loops are kept. In models Nr. 4 and 5 also the assumptions on BSM particles in loops are removed, which results in a fit also including the effective coupling scale factors κ_γ, $\kappa_{(Z\gamma)}$ and κ_g. Model Nr. 4 unifies all down-type fermion couplings, while model Nr. 5 separates the second and third generation down-type fermions. In general in these extended models the couplings to W and Z as well as the loop induced couplings to photons and gluons are expected to be measured with ~4-5% precision assuming 3000 fb^{-1}, while the fermion couplings have precisions of ~7-10%. Compared to the expectation for 300 fb^{-1} this is an improvement of up to a

factor of 2.

Without assumptions on the total width only ratios of coupling scale factors can be determined at the LHC. In this case $\sigma \cdot B\,(i \to H \to f)$ for all signal channels is a function of products of ratios $\lambda_{XY} = \kappa_X/\kappa_Y$ of coupling scale factors giving the propotionality $\sigma \cdot B\,(i \to H \to f) \sim \lambda_{iY}^2 \cdot \kappa_{YY'}^2 \cdot \lambda_{fY}^2$, where $\kappa_{YY'} = \kappa_Y \cdot \kappa_{Y'}/\kappa_H$ is a suitable chosen overall scale parameter common to all signal channels and λ_{iY} and λ_{fY} are the coupling scale factor ratios involving the initial, respectively final state, particles. In addition to avoiding the assumption on the total width, ratios of coupling scale factors also have the advantage that many experimental and theoretical systematic uncertainties cancel.

The expected precision on ratios of coupling parameters is given in Table 19 for selected bechmark parametrizations. Ratios involving explicitly the b-quark coupling λ_{bY} are not determined due to the absence of $H \to b\bar{b}$ projections at high luminosity. However this does not affect the other parameters in the shown benchmark models. The first four benchmarks are targeted at specific aspects of the SM: Benchmark model Nr. 1 for the ratio between fermion and gauge boson couplings, Nr. 2 for the ratio between the W- and Z-coupling, Nr. 3 for the ratio between up- and down-type fermion couplings and Nr. 4 for the ratio between second and third generation leptons. At 3000 fb^{-1} experimental uncertainties between ~1.5% and ~9% are possible for these ratios, which will allows testing the SM to a very high degree of precision. In many cases an improvement by more than a factor 2 compared to the expectation for 300 fb^{-1}is obtained. When the current theory uncertainties are taken into account these precisions on the ratios are only slightly degraded.

The experimental precisions for a fully generic benchmark parametrization, that does not need any assumptions beyond those in section 11.2, are summarized in Fig. 23 and in model Nr. 5 in Table 19. For 3000 fb^{-1} precisions range from ~2% for the best determined coupling scale factor ratios between the electroweak bosons to ~6-7% for the ratios involving gluons and the second and third generation fermions (~3-10% including current theory uncertainties). Only the coupling ratio involving the very small loop induced $Z\gamma$ coupling is determined at the 30% level even with 3000 fb^{-1}. Compared to the precisions at 300 fb^{-1} an improvement by a factor 2-3 is reached with 3000 fb^{-1}.

11.4 Relation of Higgs Coupling and particle mass

In order to determine the mass dependence of the Higgs boson couplings, mass-scaled couplings are defined as in Eqn. (19) and (20) in Ref. [45] as

$$Y_f = \kappa_f \frac{m_f}{v} \tag{4}$$

for the fermions f=μ, τ and t and

$$Y_V = \kappa_V \frac{m_V}{v} \tag{5}$$

for the weak bosons V=W and Z. The fit results for a fully generic model without assumptions (Table 19, model Nr. 6) are used. The fit parameters are ratios to κ_γ, with $\kappa_\gamma\kappa_\gamma/\kappa_H$ as the overall scale parameter. Hence the fitted coupling scale factor ratios are $\lambda_{\mu\gamma} = \kappa_\mu/\kappa_\gamma$, $\lambda_{\tau\gamma} = \kappa_\tau/\kappa_\gamma$, $\lambda_{t\gamma} = \kappa_t/\kappa_\gamma$, $\lambda_{W\gamma} = \kappa_W/\kappa_\gamma$, $\lambda_{Z\gamma} = \kappa_Z/\kappa_\gamma$, $\lambda_{g\gamma} = \kappa_g/\kappa_\gamma$, $\lambda_{(Z\gamma)\gamma} = \kappa_{(Z\gamma)}/\kappa_\gamma$, and $\kappa_{\gamma\gamma} = \kappa_\gamma\kappa_\gamma/\kappa_H$. Fig. 24 shows the mass-scaled coupling ratios Y_i/κ_γ, calculated from the ratios $\lambda_{i\gamma} = \kappa_i/\kappa_\gamma$, as a function of the mass for particle i. For completeness, the uncertainty on the gluon-coupling ratio measurement κ_g/κ_γ, which can be used as an indirect measurement of the top-coupling through the $gg \to H$ process, is also shown next to the expected measurement for Y_t/κ_γ which uses the direct ttH process. The uncertainty on the coupling ratio $\kappa_{(Z\gamma)}/\kappa_\gamma$ is not shown.

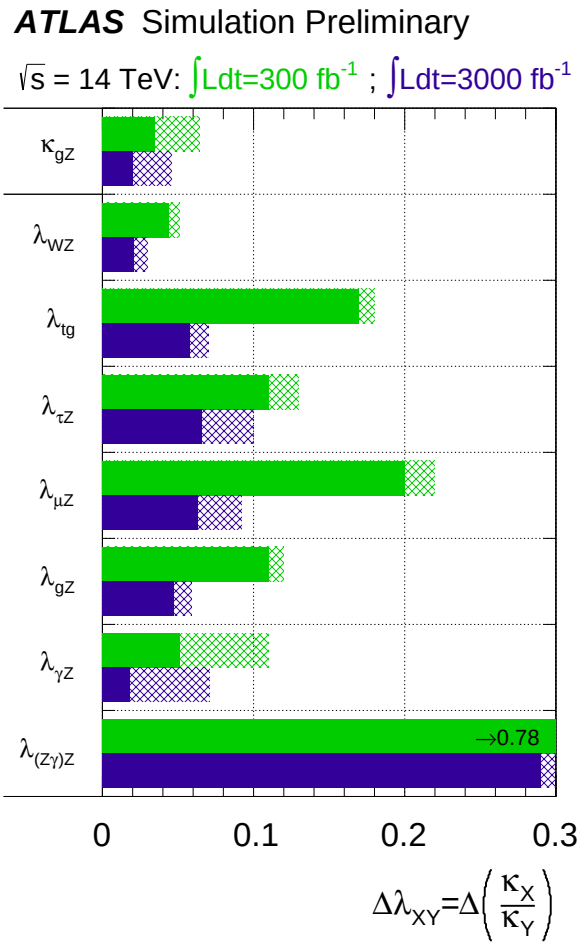

Figure 23: Relative uncertainty on the expected precision for the determination of coupling scale factor ratios λ_{XY} in a generic fit without assumptions, assuming a SM Higgs Boson with a mass of 125 GeV and LHC at 14 TeV, 300 fb^{-1} and 3000 fb^{-1}. The hashed areas indicate the increase of the estimated error due to current theory systematics uncertainties. The numerical values can be found in model Nr. 5 in Table 19.

Nr.	Coupling	300 fb^{-1} Theory unc.:			3000 fb^{-1} Theory unc.:		
		All	Half	None	All	Half	None
1	κ	3.2%	2.7%	2.5%	2.5%	1.9%	1.6%
2	$\boldsymbol{\kappa_V = \kappa_Z = \kappa_W}$	3.3%	2.8%	2.7%	2.6%	1.9%	1.7%
	$\boldsymbol{\kappa_F} = \kappa_t = \kappa_b = \kappa_\tau = \kappa_\mu$	8.6%	7.5%	7.1%	4.1%	3.5%	3.2%
3	κ_Z	8.4%	7.3%	6.8%	6.3%	5.0%	4.6%
	κ_W	8.0%	6.7%	6.2%	6.1%	4.8%	4.3%
	κ_t	11%	9.0%	8.3%	7.0%	5.6%	5.1%
	$\boldsymbol{\kappa_{d3}} = \kappa_\tau = \kappa_b$	18%	14%	13%	14%	11%	10%
	κ_μ	22%	20%	20%	10%	8.1%	7.5%
4	κ_Z	8.0%	7.0%	6.6%	5.2%	4.3%	4.0%
	κ_W	7.7%	6.8%	6.5%	4.9%	4.2%	3.9%
	κ_t	19%	18%	18%	7.7%	6.7%	6.3%
	$\boldsymbol{\kappa_d} = \kappa_\tau = \kappa_\mu = \kappa_b$	16%	13%	12%	11%	8.2%	7.2%
	κ_g	8.9%	7.9%	7.5%	4.3%	3.8%	3.6%
	κ_γ	13%	9.3%	7.8%	9.3%	5.9%	4.2%
	$\kappa_{Z\gamma}$	79%	78%	78%	30%	30%	29%
5	κ_Z	8.1%	7.1%	6.7%	6.2%	4.9%	4.4%
	κ_W	7.9%	6.9%	6.5%	5.9%	4.8%	4.4%
	κ_t	22%	20%	20%	10%	8.4%	7.8%
	$\boldsymbol{\kappa_{d3}} = \kappa_\tau = \kappa_b$	18%	15%	13%	15%	11%	9.7%
	κ_μ	23%	21%	21%	11%	8.5%	7.6%
	κ_g	11%	9.1%	8.5%	6.9%	5.5%	4.9%
	κ_γ	13%	9.3%	7.8%	9.4%	6.1%	4.6%
	$\kappa_{Z\gamma}$	79%	78%	78%	30%	30%	29%

Table 18: Expected precision on Higgs coupling scale factors with 300 and 3000 fb^{-1} at $\sqrt{s} = 14$ TeV for selected parametrizations, assuming no new contributions to the Higgs total width beyond those in the Standard Model. The Higgs total width can still differ from its expected value in the Standard Model in the absence of any new decay modes if any of its couplings to SM particles differ from their expected values. Additional parametrizations explicitly including the b-quark coupling scale factor κ_b are possible in principle, but are not studied at the moment in the absence of $H \to b\bar{b}$ projections at high luminosity. The coupling scale factor $\boldsymbol{\kappa_V}$ represents the gauge bosons W and Z, $\boldsymbol{\kappa_F}$ all fermions, and $\boldsymbol{\kappa_d}$ and $\boldsymbol{\kappa_{d3}}$ all, respectively third generation, down-type fermions.

Nr.	Coupling ratio	300 fb^{-1} Theory unc.:			3000 fb^{-1} Theory unc.:		
		All	Half	None	All	Half	None
1	κ_{VV}	7.6%	7.1%	6.9%	4.1%	3.3%	3.0%
	λ_{FV}	8.5%	7.7%	7.5%	3.7%	3.2%	3.0%
2	κ_{ZZ}	10%	9.3%	8.9%	6.1%	4.7%	4.1%
	λ_{WZ}	4.7%	4.0%	3.7%	2.8%	2.0%	1.6%
	λ_{FZ}	9.4%	8.6%	8.4%	4.5%	3.9%	3.6%
3	κ_{uu}	13%	11%	10%	6.3%	5.0%	4.5%
	λ_{Vu}	10%	8.9%	8.5%	4.6%	3.8%	3.5%
	λ_{du}	11%	9.1%	8.2%	7.1%	5.6%	4.9%
4	$\kappa_{\tau\tau}$	22%	18%	16%	17%	14%	12%
	$\lambda_{V\tau}$	12%	11%	9.8%	9.3%	7.2%	6.4%
	$\lambda_{q\tau}$	12%	9.6%	8.7%	9.1%	7.0%	6.1%
	$\lambda_{\mu\tau}$	24%	22%	21%	12%	9.6%	8.8%
5	κ_{gZ}	6.4%	4.4%	3.5%	4.6%	2.9%	2.0%
	λ_{WZ}	5.1%	4.6%	4.4%	3.0%	2.3%	2.1%
	λ_{tg}	18%	18%	17%	7.0%	6.1%	5.8%
	$\lambda_{\tau Z}$	13%	11%	11%	10%	7.6%	6.6%
	$\lambda_{\mu Z}$	22%	21%	20%	9.2%	7.2%	6.3%
	λ_{gZ}	12%	11%	11%	5.9%	5.0%	4.7%
	$\lambda_{\gamma Z}$	11%	6.9%	5.1%	7.1%	3.9%	1.8%
	$\lambda_{(Z\gamma)Z}$	78%	78%	78%	30%	29%	29%
6	$\kappa_{\gamma\gamma}$	22%	16%	13%	14%	8.3%	5.4%
	$\lambda_{Z\gamma}$	11%	6.9%	5.1%	7.1%	3.9%	1.8%
	$\lambda_{W\gamma}$	11%	7.3%	5.6%	7.4%	4.2%	2.2%
	$\lambda_{t\gamma}$	27%	23%	21%	14%	9.7%	7.7%
	$\lambda_{\tau\gamma}$	15%	12%	11%	10%	7.7%	6.7%
	$\lambda_{\mu\gamma}$	21%	20%	20%	7.2%	6.6%	6.3%
	$\lambda_{g\gamma}$	18%	13%	11%	11%	6.8%	5.0%
	$\lambda_{(Z\gamma)\gamma}$	77%	76%	76%	29%	29%	29%

Table 19: Expected precision on ratios of Higgs coupling scale factors with 300 and 3000 fb^{-1} at $\sqrt{s}$ = 14 TeV for selected benchmark parametrizations without assumptions on the Higgs total width. In model Nr. 5 (6), the ratio of the b-quark coupling to the Z boson (photon) coupling, bZ ($b\gamma$), is not determined due to the absence of $H \to b\bar{b}$ projections at high luminosity. However this does not affect the other parameters in the models shown.

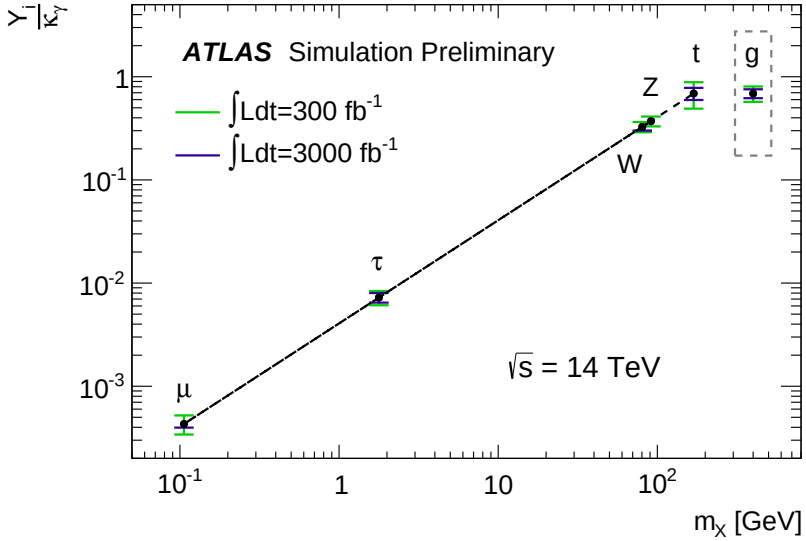

Figure 24: Fit results for mass-scaled coupling ratios $Y_f/\kappa_\gamma = \kappa_f/\kappa_\gamma \frac{m_f}{v}$ for fermions and $Y_V/\kappa_\gamma = \kappa_V/\kappa_\gamma \frac{m_V}{v}$ for weak bosons as a function of the particle mass, assuming 300 fb^{-1} and 3000 fb^{-1} at 14 TeV and a SM Higgs Boson with a mass of 125 GeV. For completeness, the uncertainty on the gluon-coupling ratio measurement κ_g/κ_γ, which can be used as an indirect measurement of the top-coupling through the $gg \to H$ process, is also shown next to the expected measurement for Y_t/κ_γ which uses the direct ttH process. The uncertainty on the coupling ratio $\kappa_{(Z\gamma)}/\kappa_\gamma$ is not shown. The relative uncertainties on the ratios can be found in model Nr. 6 in Table 19.

12 Conclusions

Several new Higgs boson production and decay modes can be observed by the ATLAS detector with 3000 fb^{-1} at the HL-LHC compared to a sample of 300 fb^{-1} that would be accumulated before the Phase-II upgrades, and the precision of all channels can be improved. Compared to previous studies [1], different Higgs production modes are explored for several final states, $\gamma\gamma$, ZZ, WW. Results for the $\mu\mu$ channel have also been updated, and the expectation for the $Z\gamma$ final state included. These two rare decay modes can only be studied at HL-LHC. Additional constraints on the Higgs boson width have been explored, from ZH production with $H \to$ invisible particles, and by using a novel measurement of the Higgs width from the interference in $H \to \gamma\gamma$. New results on the more complicated $\tau\tau$ and $b\bar{b}$ decay modes are under study. The projected precisions on cross section times branching ratio measurements are interpreted as constraints on Higgs boson couplings to fermions and bosons in a variety of models.

References

[1] ATLAS Collaboration, ATL-PHYS-PUB-2012-004. https://cdsweb.cern.ch/record/1484890.

[2] R. Aleksan et al., CERN-ESG-005. http://europeanstrategygroup.web.cern.ch/europeanstrategygroup/Briefing_book.pdf.

[3] ATLAS Collaboration, CERN-LHCC-2012-022. https://cds.cern.ch/record/1502664.

[4] ATLAS Collaboration, ATL-PHYS-PUB-2013-004. https://cds.cern.ch/record/1527529.

[5] ATLAS Collaboration, ATL-PHYS-PUB-2013-009. https://cds.cern.ch/record/1604420.

[6] L. J. Dixon and Y. Li, arXiv:1305.3854 [hep-ph]. Submitted to PRL.

[7] S. P. Martin, arXiv:1303.3342 [hep-ph].

[8] ATLAS Collaboration, ATLAS-CONF-2013-013 (2013) . https://cds.cern.ch/record/1523699.

[9] S. Dittmaier, S. Dittmaier, C. Mariotti, G. Passarino, R. Tanaka, et al., arXiv:1201.3084 [hep-ph].

[10] ATLAS Collaboration, Phys.Lett. **B716** (2012) 1–29, arXiv:1207.7214 [hep-ex].

[11] ATLAS Collaboration, arXiv:0901.0512 [hep-ex].

[12] ATLAS Collaboration, ATLAS-CONF-2013-009. https://cds.cern.ch/record/1523683.

[13] V. Barger, M. Ishida, and W.-Y. Keung, Phys.Rev.Lett. **108** (2012) 261801, arXiv:1203.3456 [hep-ph].

[14] ATLAS Collaboration, Tech. Rep. ATLAS-CONF-2013-072, CERN, Geneva, Jul, 2013. http://cds.cern.ch/record/1562925/.

[15] CMS Collaboration, Tech. Rep. CMS-PAS-HIG-13-016, CERN, Geneva, Jul, 2013. https://cds.cern.ch/record/1558930/.

[16] ATLAS Collaboration, ATLAS-CONF-2013-030 (2013) . https://cds.cern.ch/record/1527126.

[17] ATLAS Collaboration, ATLAS-CONF-2012-094. https://cds.cern.ch/record/1460440.

[18] ATLAS Collaboration, ATLAS-CONF-2013-010. https://cds.cern.ch/record/1523695.

[19] J. F. Gunion and X.-G. He, Phys.Rev.Lett. **76** (1996) 4468–4471, arXiv:hep-ph/9602226 [hep-ph].

[20] ATLAS Collaboration, CERN-OPEN-2008-020 (2008).

[21] ATLAS Collaboration, ATLAS-CONF-2013-011 (2013). https://cds.cern.ch/record/1523696.

[22] B. Patt and F. Wilczek, arXiv:hep-ph/0605188.

[23] P. J. Fox, R. Harnik, J. Kopp, and Y. Tsai, Phys.Rev. **D85** (2012) 056011, arXiv:1109.4398 [hep-ph].

[24] A. Djouadi, O. Lebedev, Y. Mambrini, and J. Quevillon, Phys.Lett. **B709** (2012) 65–69, arXiv:1112.3299 [hep-ph].

[25] L. Lopez-Honorez, T. Schwetz, and J. Zupan, Phys.Lett. **B716** (2012) 179–185, arXiv:1203.2064 [hep-ph].

[26] J. Angle *et al.* (XENON10 Collaboration), Phys. Rev. Lett. **107** (2011) 051301.

[27] E. Aprile *et al.* (XENON100 Collaboration), Phys. Rev. Lett. **109** (2012) 181301.

[28] K. Arisaka for XENON1T Collaboration, Snowmass Cosmic Frontier Workshop, March 6-8, 2013.

[29] G. Angloher et al., Eur. Phys. J. C **72** (2012) 1971.

[30] R. Bernabei et al. (DAMA), Eur. Phys. J. **C56** (2008) 333.

[31] C. Aalseth, P. Barbeau, J. Colaresi, J. Collar, J. Diaz Leon, et al., Phys.Rev.Lett. **107** (2011) 141301, arXiv:1106.0650 [astro-ph.CO].

[32] P. Fox, J. Kopp, M. Lisanti, and N. Weiner, Phys. Rev. D **85** (2012) 036008.

[33] R. Agnese *et al.* (CDMS Collaboration), Phys. Rev. Lett. **111** (2013) 251301.

[34] S. Kanemura, S. Matsumoto, T. Nabeshima, and N. Okada, Phys. Rev. **D82** (2010) 055026.

[35] ATLAS Collaboration, arXiv:1307.1427 [hep-ex].

[36] ATLAS Collaboration, Phys. Rev. **D 86** (2012) 032003, arXiv:1207.0319 [hep-ex].

[37] ATLAS and CMS Collaborations, ATL-PHYS-PUB-2011-011, CERN-CMS-NOTE-2011-005 (2011). http://cdsweb.cern.ch/record/1375842.

[38] L. Moneta, K. Belasco, K. S. Cranmer, S. Kreiss, A. Lazzaro, et al., PoS **ACAT2010** (2010) 057, arXiv:1009.1003 [physics.data-an].

[39] K. Cranmer, G. Lewis, L. Moneta, A. Shibata, and W. Verkerke, CERN-OPEN-2012-016 (2012). http://cdsweb.cern.ch/record/1456844.

[40] W. Verkerke *et al.*,, "The roofit toolkit for data modelling." Available from http://roofit.sourceforge.net or with recent versions of the root framework available at http://root.cern.ch.

[41] LHC Higgs Cross Section Working Group, arXiv:1307.1347 [hep-ph].

[42] LHC Higgs Cross Section Working Group,. https://twiki.cern.ch/twiki/bin/view/LHCPhysics/CrossSections.

[43] Higgs cross sections for European Strategy studies in 2012 ,. https://twiki.cern.ch/twiki/bin/view/LHCPhysics/HiggsEuropeanStrategy2012.

[44] ATLAS Collaboration, ATL-PHYS-PUB-2013-xxx. InPreparation.

[45] M. Spira, R. Tanaka,. https://twiki.cern.ch/twiki/bin/view/LHCPhysics/SMInputParameter#MSbar_running_masses_for_the_qua.

A Results for all coupling fits

This appendix summarizes a large number of additional coupling scale factor fits using benchmark models with (Table 20) and without (Tables 21–23) assumptions on the total width following the recommendations in Ref. [41]. In these tables the index "V" represents the gauge bosons W and Z, "F" all fermions, "u" up-type fermions (mainly top), "d" down-type fermions, "q" quarks, "l" leptons, "2" and "3" second, respectively third, generation fermions, and "$d2$" and "$d3$" second, respectively third, generation down-type fermions. The branching ratio for invisible or undetectable Higgs decays is denoted "$\mathrm{BR}_{i,u}$".

Nr.	Coupling	300 fb^{-1}			3000 fb^{-1}		
		Theory unc.:			Theory unc.:		
		All	Half	None	All	Half	None
1	κ_Z	4.4%	3.6%	3.3%	3.2%	2.3%	1.9%
	κ_W	3.8%	3.4%	3.2%	2.7%	2.0%	1.8%
	κ_F	8.7%	7.7%	7.3%	4.1%	3.6%	3.4%
2	κ_V	7.6%	6.5%	6.1%	4.9%	4.0%	3.7%
	κ_u	8.8%	7.7%	7.2%	4.3%	3.8%	3.6%
	κ_d	15%	13%	12%	9.4%	7.8%	7.1%
3	κ_V	3.3%	2.8%	2.7%	2.6%	1.9%	1.7%
	κ_3	10%	8.5%	7.8%	5.5%	4.3%	3.8%
	κ_2	20%	20%	19%	7.0%	6.4%	6.2%
4	κ_V	3.3%	2.9%	2.7%	2.6%	2.0%	1.7%
	κ_q	12%	9.3%	8.4%	5.6%	4.4%	3.9%
	κ_τ	13%	10%	9.6%	9.6%	7.5%	6.7%
	κ_μ	20%	20%	20%	7.0%	6.5%	6.2%
5	κ_Z	8.2%	7.2%	6.8%	5.1%	4.4%	4.1%
	κ_W	7.8%	6.6%	6.1%	5.0%	4.0%	3.7%
	κ_u	8.8%	7.8%	7.4%	4.4%	3.8%	3.6%
	κ_d	15%	13%	12%	9.5%	7.8%	7.2%
6	κ_V	6.6%	6.0%	5.8%	3.8%	3.3%	3.0%
	κ_F	13%	12%	11%	6.4%	5.6%	5.3%
	κ_g	8.8%	7.8%	7.5%	4.2%	3.6%	3.4%
	κ_γ	11%	8.2%	7.2%	5.8%	4.1%	3.3%
	$\kappa_{Z\gamma}$	77%	77%	77%	30%	29%	29%

Table 20: Expected precision on Higgs couplings with 300 and 3000 fb^{-1} at $\sqrt{s}$ = 14 TeV, assuming no new contributions to the Higgs total width beyond those in the Standard Model. The Higgs total width can still differ from its expected value in the Standard Model in the absence of any new decay modes if any of its couplings to SM particles differ from their expected values. Additional parametrizations including a free b-quark coupling are possible in principle, but are not studied at the moment in the absence of $H \to b\bar{b}$ projections at high luminosity.

Nr.	Parameter	300 fb^{-1}			3000 fb^{-1}		
		Theory unc.:			Theory unc.:		
		All	Half	None	All	Half	None
1	κ_g	7.5%	5.9%	5.2%	3.5%	2.9%	2.6%
	κ_γ	9.3%	6.2%	4.8%	5.2%	3.0%	1.7%
	$\kappa_{Z\gamma}$	78%	78%	78%	30%	29%	29%
	BR$_{i,u}$	<28%	<26%	<25%	<15%	<13%	<12%

Table 21: Expected precision on the loop-induced Higgs couplings κ_g, κ_γ, and $\kappa_{Z\gamma}$, along with the expected 95% CL upper limit on the branching ratio for invisible or undetectable Higgs decays, BR$_{i,u}$, with 300 and 3000 fb^{-1} at $\sqrt{s}$ = 14 TeV. Other couplings to massive particles are assumed to be equal to their SM values, but no other assumptions are made relating to the Higgs total width.

Nr.	Coupling ratio	300 fb^{-1} Theory unc.:			3000 fb^{-1} Theory unc.:		
		All	Half	None	All	Half	None
1	λ_{V3}	10%	8.7%	8.2%	4.9%	4.0%	3.7%
	κ_{33}	13%	11%	9.9%	6.6%	5.3%	4.7%
	λ_{23}	24%	22%	21%	9.4%	8.0%	7.4%
2	κ_{ZZ}	11%	10%	9.8%	6.3%	5.1%	4.6%
	λ_{WZ}	4.7%	4.0%	3.8%	2.8%	2.0%	1.6%
	λ_{uZ}	11%	10%	9.7%	5.2%	4.5%	4.3%
	λ_{dZ}	11%	9.6%	9.1%	6.4%	5.0%	4.5%
3	κ_{ZZ}	11%	11%	10%	6.4%	5.2%	4.8%
	λ_{WZ}	4.7%	4.0%	3.8%	2.8%	2.0%	1.6%
	λ_{uZ}	12%	11%	10%	5.5%	4.8%	4.6%
	λ_{d3Z}	13%	11%	10%	9.6%	7.4%	6.5%
	λ_{d2Z}	21%	20%	19%	7.8%	6.6%	6.1%
4	κ_{ZZ}	11%	11%	10%	6.4%	5.2%	4.8%
	λ_{WZ}	4.7%	4.0%	3.8%	2.8%	2.0%	1.6%
	λ_{tZ}	12%	11%	11%	5.4%	4.8%	4.5%
	$\lambda_{\tau Z}$	13%	11%	10%	9.5%	7.4%	6.5%
	$\lambda_{\mu Z}$	21%	20%	19%	7.8%	6.6%	6.1%

Table 22: Expected precision on ratios of Higgs couplings with 300 and 3000 fb^{-1} at $\sqrt{s}$ = 14 TeV, without any assumption on the Higgs total width. In model Nr. 4, the ratio of the b-quark coupling to the Z boson coupling, bZ, is not determined due to the absence of $H \to b\bar{b}$ projections at high luminosity. However this does not affect the other parameters in the models shown.

Nr.	Coupling ratio	300 fb^{-1} Theory unc.:			3000 fb^{-1} Theory unc.:		
		All	Half	None	All	Half	None
1	κ_{VV}	9.2%	8.8%	8.6%	5.1%	4.2%	3.9%
	λ_{FV}	10%	9.2%	8.9%	4.9%	4.1%	3.9%
	λ_{gV}	10%	9.6%	9.4%	4.3%	4.0%	3.9%
	$\lambda_{\gamma V}$	9.5%	6.3%	4.8%	5.6%	3.1%	1.7%
	$\lambda_{(Z\gamma)V}$	77%	77%	76%	29%	29%	29%
2	κ_{ZZ}	11%	11%	10%	6.5%	5.3%	4.8%
	λ_{WZ}	5.1%	4.6%	4.4%	3.0%	2.4%	2.1%
	λ_{uZ}	23%	21%	21%	9.8%	8.2%	7.6%
	λ_{d3Z}	13%	11%	11%	10%	7.6%	6.6%
	λ_{d2Z}	22%	21%	20%	9.1%	7.1%	6.3%
	λ_{gZ}	12%	11%	11%	5.9%	5.0%	4.7%
	$\lambda_{\gamma Z}$	11%	6.8%	5.0%	7.1%	3.9%	1.8%
	$\lambda_{(Z\gamma)Z}$	77%	77%	76%	29.7%	29.2%	29.1%
3	κ_{ZZ}	11%	11%	10%	6.5%	5.3%	4.8%
	λ_{WZ}	5.1%	4.6%	4.4%	3.0%	2.4%	2.1%
	λ_{tZ}	23%	21%	21%	9.8%	8.2%	7.6%
	$\lambda_{\tau Z}$	13%	11%	11%	10%	7.6%	6.6%
	$\lambda_{\mu Z}$	22%	21%	20%	9.1%	7.1%	6.3%
	λ_{gZ}	12%	11%	11%	5.9%	5.0%	4.7%
	$\lambda_{\gamma Z}$	11%	6.8%	5.0%	7.1%	3.9%	1.8%
	$\lambda_{(Z\gamma)Z}$	77%	77%	76%	30%	29%	29%
4	κ_{ZZ}	11%	10%	9.9%	6.4%	5.1%	4.6%
	λ_{WZ}	5.1%	4.6%	4.4%	3.0%	2.4%	2.1%
	λ_{uZ}	21%	20%	19%	9.3%	7.7%	7.1%
	λ_{dZ}	12%	10%	9.3%	7.6%	5.5%	4.6%
	λ_{gZ}	11%	10%	10%	5.5%	4.7%	4.4%
	$\lambda_{\gamma Z}$	10%	6.7%	5.0%	6.9%	3.8%	1.8%
	$\lambda_{(Z\gamma)Z}$	77%	77%	76%	30%	29%	29%
5	κ_{gZ}	6.2%	4.3%	3.5%	4.5%	2.8%	2.0%
	λ_{WZ}	5.0%	4.6%	4.4%	3.0%	2.4%	2.1%
	λ_{ug}	18%	17%	17%	6.9%	6.0%	5.7%
	λ_{dZ}	12%	10%	9.3%	7.6%	5.5%	4.6%
	λ_{gZ}	11%	10%	10%	5.6%	4.7%	4.4%
	$\lambda_{\gamma Z}$	10%	6.8%	5.1%	7.0%	3.8%	1.8%
	$\lambda_{(Z\gamma)Z}$	77%	77%	76%	30%	29%	29%

Table 23: Expected precision on ratios of Higgs couplings with 300 and 3000 fb^{-1} at $\sqrt{s}$ = 14 TeV, without any assumption on the Higgs total width. In model Nr. 3, the ratio of the b-quark coupling to the Z boson coupling, bZ, is not determined due to the absence of $H \to b\bar{b}$ projections at high luminosity. However this does not affect the other parameters in the models shown.